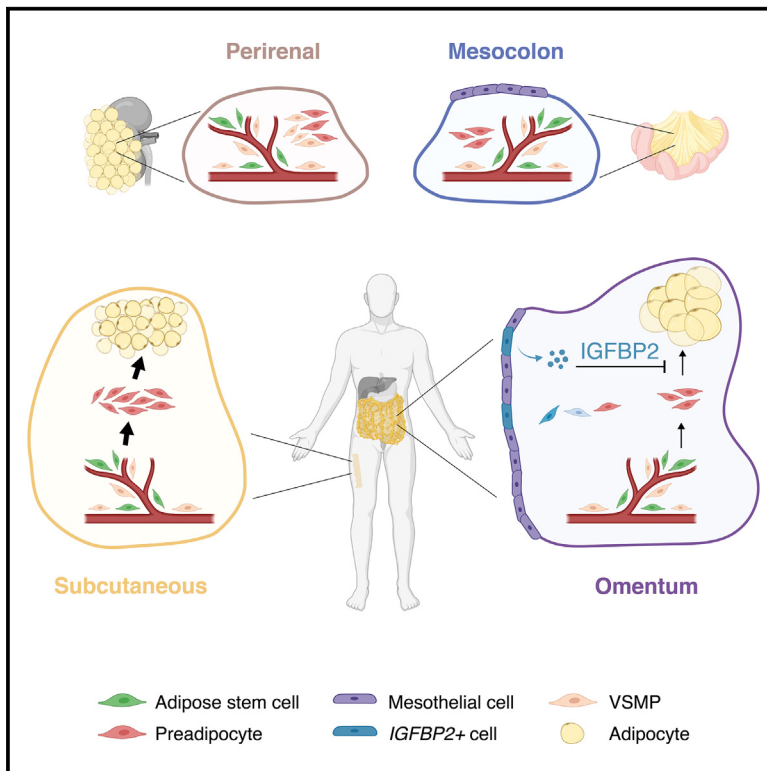


Cell Metabolism

A human omentum-specific mesothelial-like stromal population inhibits adipogenesis through IGFBP2 secretion

Graphical abstract



Authors

Radiana Ferrero, Pernille Yde Rainer, Marie Rumpler, ..., Kai-Uwe Schladraff, Carles Canto, Bart Deplancke

Correspondence

bart.deplancke@epfl.ch

In brief

Ferrero, Rainer, et al. perform single-cell and bulk RNA-seq of >30 samples across four human adipose depots. Different Lin⁻ stromal cell subpopulations were transcriptionally cataloged, isolated, and functionally characterized, uncovering an omental-specific, high *IGFBP2*-expressing stromal population able to repress adipogenesis of adipose stem and progenitor cells via integrin receptor signaling.

Highlights

- A single-cell transcriptomic atlas integrating Lin⁻ SVF cells from four different human adipose depots
- In-depth transcriptional analysis of stromal populations across four human adipose depots
- Adipogenic characterization of five stromal populations across three human adipose depots
- Omental-specific cells characterized by high *IGFBP2* expression repress adipogenesis



Article

A human omentum-specific mesothelial-like stromal population inhibits adipogenesis through IGFBP2 secretion

Radiana Ferrero,^{1,2,7} Pernille Yde Rainer,^{1,2,7} Marie Rumpler,^{1,2} Julie Russeil,¹ Magda Zachara,¹ Joern Pezoldt,^{1,2} Guido van Mierlo,^{1,2} Vincent Gardeux,^{1,2} Wouter Saelens,^{1,2} Daniel Alpern,^{1,2} Lucie Favre,^{3,5} Nathalie Vionnet,^{3,5} Styliani Mantziari,^{4,5} Tobias Zingg,^{4,5} Nelly Pitteloud,^{3,5} Michel Suter,^{4,5} Maurice Matter,^{4,5} Kai-Uwe Schladraff,⁶ Carles Canto,^{1,2,8} and Bart Deplancke^{1,2,8,9,*}

¹Laboratory of Systems Biology and Genetics, Institute of Bioengineering, School of Life Sciences, Ecole Polytechnique Fédérale de Lausanne (EPFL), 1015 Lausanne, Switzerland

²Swiss Institute of Bioinformatics, 1015 Lausanne, Switzerland

³Department of Endocrinology, Diabetology and Metabolism, University Hospital of Lausanne (CHUV), 1011 Lausanne, Switzerland

⁴Department of Visceral Surgery, University Hospital of Lausanne (CHUV), Lausanne 1011, Switzerland

⁵Faculty of Biology and Medicine, University of Lausanne, Lausanne 1005, Switzerland

⁶Concept-Clinic, 1205 Geneva, Switzerland

⁷These authors contributed equally

⁸Senior author

⁹Lead contact

*Correspondence: bart.deplancke@epfl.ch
<https://doi.org/10.1016/j.cmet.2024.04.017>

SUMMARY

Adipose tissue plasticity is orchestrated by molecularly and functionally diverse cells within the stromal vascular fraction (SVF). Although several mouse and human adipose SVF cellular subpopulations have by now been identified, we still lack an understanding of the cellular and functional variability of adipose stem and progenitor cell (ASPC) populations across human fat depots. To address this, we performed single-cell and bulk RNA sequencing (RNA-seq) analyses of >30 SVF/Lin[−] samples across four human adipose depots, revealing two ubiquitous human ASPC (hASPC) subpopulations with distinct proliferative and adipogenic properties but also depot- and BMI-dependent proportions. Furthermore, we identified an omental-specific, high *IGFBP2*-expressing stromal population that transitions between mesothelial and mesenchymal cell states and inhibits hASPC adipogenesis through IGFBP2 secretion. Our analyses highlight the molecular and cellular uniqueness of different adipose niches, while our discovery of an anti-adipogenic IGFBP2+ omental-specific population provides a new rationale for the biomedically relevant, limited adipogenic capacity of omental hASPCs.

INTRODUCTION

Our understanding of key adipose tissue (AT) phenotypes, such as turnover and expansion dynamics in response to metabolic alterations, is still limited, especially in human AT. Further, these phenotypes vary according to the AT's anatomical location. This is illustrated by the frequent opposition of the overgrown “metabolically healthy” subcutaneous (SC) AT to the “unhealthy” visceral one. However, the terms “visceral” and “SC” underlie several finer anatomic locations and, with them, more fine-grained characteristics and links to disease.¹ For instance, fat accumulation in particular anatomic locations has stronger links to obesity-related insulin resistance.² In part, this has been proposed to be related to the intrinsic ability of different depots to increase their size via the formation of new adipocytes (hyperplasia) and/or via (over)growth of their existing adipocytes

(hypertrophy).^{2,3} Although it is well accepted that human ATs from distinct anatomical locations expand differently,³ little is known about what causes these phenotypic divergences. One possibility is that these differences could be partially driven by variation in the cellular composition of the stromal vascular fraction (SVF) across depots and, more specifically, of adipose stem and progenitor cells (ASPCs). Single-cell RNA sequencing (scRNA-seq) atlases of whole human AT have provided insights into the heterogeneity of human ASPCs (hASPCs).^{4–6} However, these scRNA-seq studies focused on the two most studied ATs: the SC and the omentum (OM), the main visceral AT in humans. Hence, similarities and/or differences in hASPC composition beyond the SC and OM depots remain elusive.

Studies in mice indicate that ASPCs are highly heterogeneous across depots but can be classified into at least three major subpopulations, characterized by specific cell surface markers and



different functional properties.^{4,5,7–11} For example, *Dpp4+* (or *Ly6c+*) cells represent adipose stem cells (ASCs), a pool of multipotent mesenchymal stem cells that commit to adipogenesis when exposed to the right mix of factors. By contrast, *Icam1+* (or *Aoc3+*) cells can be classified as pre-adipocytes (PreAs), showing a lower proliferation capacity and a more committed adipogenic state compared with ASCs. Finally, a subset of cells characterized by high expression of *F3* were termed adipogenesis-regulatory cells (Aregs) due to their ability to regulate the differentiation capacity of other ASCs.^{7,12,13} Initial efforts to functionally characterize hASPC subpopulations suggested some similarities to the ones identified in mice, with the *DPP4+* ASCs being highly proliferative and less adipogenic than the *ICAM1+* ASCs.⁴ Together, these findings suggest that mouse and hASPCs might share similar populations. Yet, to date, no systematic, functional characterization of hASPC heterogeneity and behavior has been performed across several human adipose depots.

Here, we provide a comprehensive overview of gene expression profiles of SVF-adherent cells over 30 human donors in four major human depots: SC, perirenal (PR), OM, and mesocolic (MC; the mesenteric fat linked to the colon) AT, combined with scRNA-seq data on ~34,000 non-immune (CD45[−]) and non-endothelial (CD31[−]) SVF cells (SVF/Lin[−]). We analyzed the main hASPC subpopulations that are common and divergent across depots, as well as their transcriptional and functional characteristics. Furthermore, we established a sorting strategy to isolate, quantify, and characterize different cellular subpopulations in SC, OM, and PR depots with regard to their adipogenic potential and proliferation abilities. Finally, we identified a new and OM-specific cell population that inhibits the adipogenic differentiation of hASPCs and hinted at its biomedical relevance by uncovering a significant correlation between inferred insulin-like growth factor binding protein (*IGFBP2*)-expressing (*IGFBP2+*) cell abundance and BMI.

RESULTS

Human SVF cells exhibit depot-dependent differences in their *in vitro* adipogenic potential and transcriptome

To functionally characterize stromal cells, including hASPCs, across distinct human adipose depots, we isolated SVFs from

SC (20 donors), PR (8 donors), OM (19 donors), and MC (4 donors) AT (Table S1). SVF-adherent cells were grown and, once confluent, exposed to an adipogenic cocktail for 14 days (Figure 1A; see STAR Methods). Staining for lipid droplets (LDs) revealed that, consistent with previous findings,¹⁴ cells from ATs outside the peritoneal cavity (SC and PR) formed mature adipocytes (Figures 1B and 1C). Conversely, cells from intraperitoneal depots (OM and MC) grew slowly and barely formed LDs under adipogenic differentiation conditions (Figures 1B, 1C, and S1A–S1C). Interestingly, freshly isolated PR cells showed the highest adipogenic potential *in vitro* (Figures 1B and 1C). However, at longer times/passages, their level of differentiation was similar to that of SC cells (Figure S1B). Furthermore, all depots showed high inter-individual variation in their stromal cells' ability to differentiate (Figure 1D). Finally, we evaluated possible correlations between our experimental adiposcore (Figure 1D; see STAR Methods) and physiological parameters such as BMI, age, and sex of the donors but found no correlations except for a tendency for PR cells to be less adipogenic in women and elderly people (Figures S1D–S1H). However, our cohort's demographic characteristics could bias these observations (Figure S1D; Tables S1 and S2), as sample donors were mainly young and people with obesity, and only a relatively small proportion of PR samples were analyzed ($n = 8$).

To explore if the different adipogenic capacity between depots was reflected in their transcriptomes, we performed bulk RNA barcoding and sequencing (BRB-seq)¹⁵ of SVF-adherent cells from different individuals and depots at the undifferentiated state (t0) and after 14 days of adipogenic differentiation (t14) (SC $n = 22$, OM $n = 16$, PR $n = 8$, MC $n = 4$). The major source of variation was explained by the exposure to the adipogenic cocktail, followed by the anatomic origin of the cells (Figures 1E and S1I–S1M). All samples at t0 highly expressed *THY1*, a well-known mesenchymal marker,¹⁶ except OM samples in which it was less expressed (Figure S1N). The exposure to a differentiation cocktail induced genes related to extracellular remodeling, insulin response, and positive regulation of fat cell differentiation in all depots (Figures 1F, S1O, and S1P), suggesting that they can engage to some degree the adipogenic program. However, adipogenesis-related terms were notably enriched in SC and PR compared with OM and MC (Figures 1F, S1O, and S1P). In addition, late adipogenesis markers were solely up-regulated in PR

(B) Representative fluorescence microscopy images of SVF-adherent cells after differentiation; yellow, lipids; blue, DNA. Scale bars, 1 μ m.

(C) Adiposcore of SVF-adherent cells in (B); $n = 14$ –22, 4–5 donors, 3–5 independent wells.

(D) Adiposcore distribution across donors and depot; subcutaneous (SC), 20 donors (D); perirenal (PR), 8 donors; omental (OM), 18 donors; mesocolic (MC), 4 donors. Through the panels, B2 indicates biological replicate from the same donor, and 1 year (1y) indicates same donor 1-year post-surgery. In all cases, 4 independent wells/donor were evaluated.

(E) t-SNE based on the transcriptomic data of SVF-adherent cells from the indicated adipose depots (SC, yellow; PR, brown; OM, purple; MC, blue) and time points (t0, light; t14, dark); $n = 12$ –61, 4–20 biological replicates, 1–4 independent replicates for each.

(F) Score for “positive regulation of fat cell differentiation,” based on the scaled expression of the corresponding GO term (GO: 0045600) of the data in (E).

(G) Relationship between the image-based adiposcore in (D) versus the transcriptomic-based “mature adipocyte score” from the same donor. Samples are grouped by depots (SC, yellow; PR, brown) and donors. Spearman correlation and adjusted R^2 of $y \sim \log(x + 1)$ (plotted orange line with 95% confidence interval) values are indicated.

(H) Enriched terms found by gene set enrichment analysis (GSEA) on the gene expression analysis results of t0 versus t14 samples for each depot of the data in (E).

(I) Top differentially expressed genes when comparing the indicated depot versus the three others at t0 of the data shown in (E).

(J) Enriched terms found by GSEA on the gene expression analysis of each depot versus the others at t14 of the data in (E).

* $p \leq 0.05$, ** $p \leq 0.01$, *** $p \leq 0.001$, **** $p \leq 0.0001$, one-way ANOVA and Tukey honest significant difference (HSD) post hoc test (C), unpaired two-sided t test (F). In the figure, all boxplots display the mean as a dark band, the box shows the 25th and 75th percentiles, while the whiskers indicate the minimum and maximum data points in the considered dataset. All bar plots display the mean value and the standard deviation from the mean as error bar.

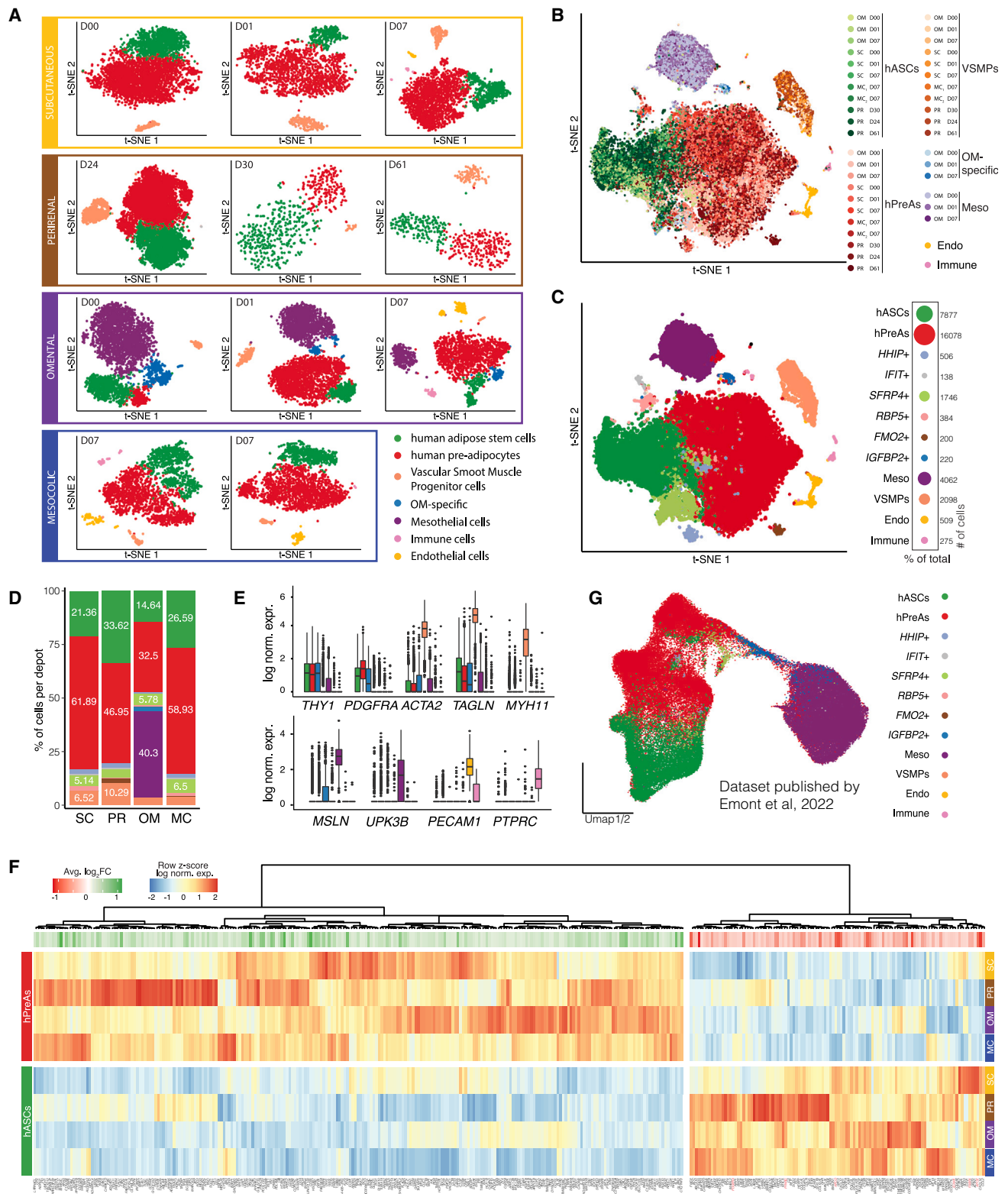


Figure 2. Human adipose stromal cells are highly heterogeneous at the single-cell level

(A) t-SNE of individual scRNA-seq datasets of SVF Lin⁻ cells isolated from SC, OM, MC, and PR adipose depots and six different donors. The identified sub-populations of hASPCs are indicated below. The number of cells per dataset from left to right was: SC: 3,929, 4,169, 2,162; PR: 8,583, 600, 509; OM: 4,262, 2,042, 2,670; MC: 2,650, 2,550.

(legend continued on next page)

and SC samples post-differentiation (Figure S1Q), supporting the very low accumulation of LDs observed in OM and MC cells. The expression of mature adipocyte markers correlated with LD accumulation, as quantified by the image-based adiposcore ($\rho = 0.81$, Figure 1G), showing that inter-individual variabilities were reflected at the transcriptomic level.

Pathway analyses showed an enrichment in lipid storage and fatty acid metabolism programs in PR and SC-derived cells upon differentiation (Figure 1H). Transcriptomic comparisons of undifferentiated cells at t0 revealed that developmental genes such as *HOXC8-10*, *HOXA9*, and *HOXD8* were highly expressed in SC samples (Figure 1I), as previously reported.^{17,18} This was further illustrated by the enrichment of numerous terms linked to morphogenesis and development compared with the other depots (Figures 1I and 1J). Interestingly, at t14, SC samples also showed enrichment of (fat) cell differentiation-related terms compared with the other depots (Figure 1J). By contrast, PR-enriched genes at t14 were related to thermogenesis and oxidative metabolism (Figure 1J). In OM samples at t14, we observed a non-adipogenic gene expression signature with positive and negative enrichment of the terms “negative regulation of differentiation” and “white fat cell differentiation,” respectively (Figure 1J). OM cells also exhibited significantly higher expression of genes linked to an inflammatory response pre- and post-exposure to an adipogenic cocktail (Figures 1J and S1R). This could be due to the OM sample demographics, primarily reflecting donors with obesity undergoing bariatric surgery (Figure S1D; Table S1), whose OM fat may exhibit signs of inflammation.^{19–21} OM cells also showed an enrichment of genes linked to the vasculature and epithelium/endothelium development (Figures 1J and S1S). Finally, MC-enriched genes were linked to endoplasmic reticulum stress, protein folding, and trafficking (Figure 1J).

Taken together, cultured SVF cells from each depot featured specific gene signatures, highlighting the regional specialization of AT. In addition, the adipogenic potential was mirrored by the up- or down-regulation of pro-adipogenic markers in extraperitoneal and intraperitoneal adipose depot-derived cells, respectively.

Human adipose-derived stromal cells are highly heterogeneous at the single-cell level

Next, we explored whether the transcriptomic and phenotypic differences across depots could be driven by cellular heterogeneity. To do so, we performed scRNA-seq of SVF Lin[−] (i.e., CD45[−]/CD31[−]) cells that were isolated from SC ($n = 3$), OM ($n = 3$), MC ($n = 2$, from the same donor), and PR ($n = 3$) adipose

samples (from 6 donors in total) (Table S2), analyzing a total of 34,126 cells (on average, ~8,500 cells per depot). We first analyzed each dataset independently, i.e., per depot and per donor, uncovering heterogeneity in and between each depot (Figure 2A). We performed a total of three independent analyses to explore if the identified subpopulations share molecular features across depots and donors. First, we calculated the overlap of the top cluster markers between datasets (Figure S2A). We found that, although the percentage of shared markers tends to be the highest within samples isolated from the same depot or donor (Figures S2B and S2C), the overlap across depots and donors is, on average, over 50% for most of the identified subpopulations (Figure S2A). This result was confirmed when projecting each dataset onto each other using scmap,²² revealing that on average more than 75% of cells from one specific population projected onto the corresponding population in other datasets, regardless of the depot of origin (Figure S2D). Finally, we integrated the data by considering each dataset as a different batch and correcting it accordingly. Once again, we observed an excellent overlap of the depot-counterpart populations in the t-distributed stochastic neighbor embedding (t-SNE) space (Figure 2B), which was further confirmed by clustering analysis (Figure 2C). Our results indicate that human adipose SVFs from SC, PR, OM, and MC depots contain at least two main hASPC subpopulations (Figures 2D and 2E), which we also captured in yet another unexplored AT, namely the AT surrounding the gallbladder in a subset of patients with morbid obesity (Figure S2E).

Based on their gene expression signatures, we labeled those two hASPC subpopulations as ASCs (hASCs) and PreAs (hPreAs) (Figures 2C and 2F). hASCs from all depots shared a gene signature enriched for *DPP4*, *CD55*, and *PI16*, and genes involved in proliferation, collagen synthesis, and stemness (Figures 2F and S2F). By contrast, hPreAs differentially expressed markers of committed adipogenic cells, such as *PPARG*, *FABP4*, *PDGFRA*, *APOC*, and *APOE*, and showed enrichment of terms linked to differentiation, commitment, and lipid transport (Figures 2F and S2F). Furthermore, our annotations are consistent with the ASPC states observed in human SC AT and predicted for OM AT using independent reference human atlases^{4–6} (Figures 2G and S2G).

In sum, we found that, at the single-cell level, two canonical hASPC populations (hASCs and hPreAs) dominate the transcriptomic landscape of the SVF and are retrieved in each analyzed depot. To our knowledge, these hASPC states have never been described for human anatomical locations beyond SC and OM.

(B) t-SNE of integrated scRNA-seq datasets across four depots and six donors (D) (Table S2; OM, $n = 3$, SC, $n = 3$, and MC, $n = 2$ (same donor) from matched donors, and PR, $n = 3$, from unmatched donors).

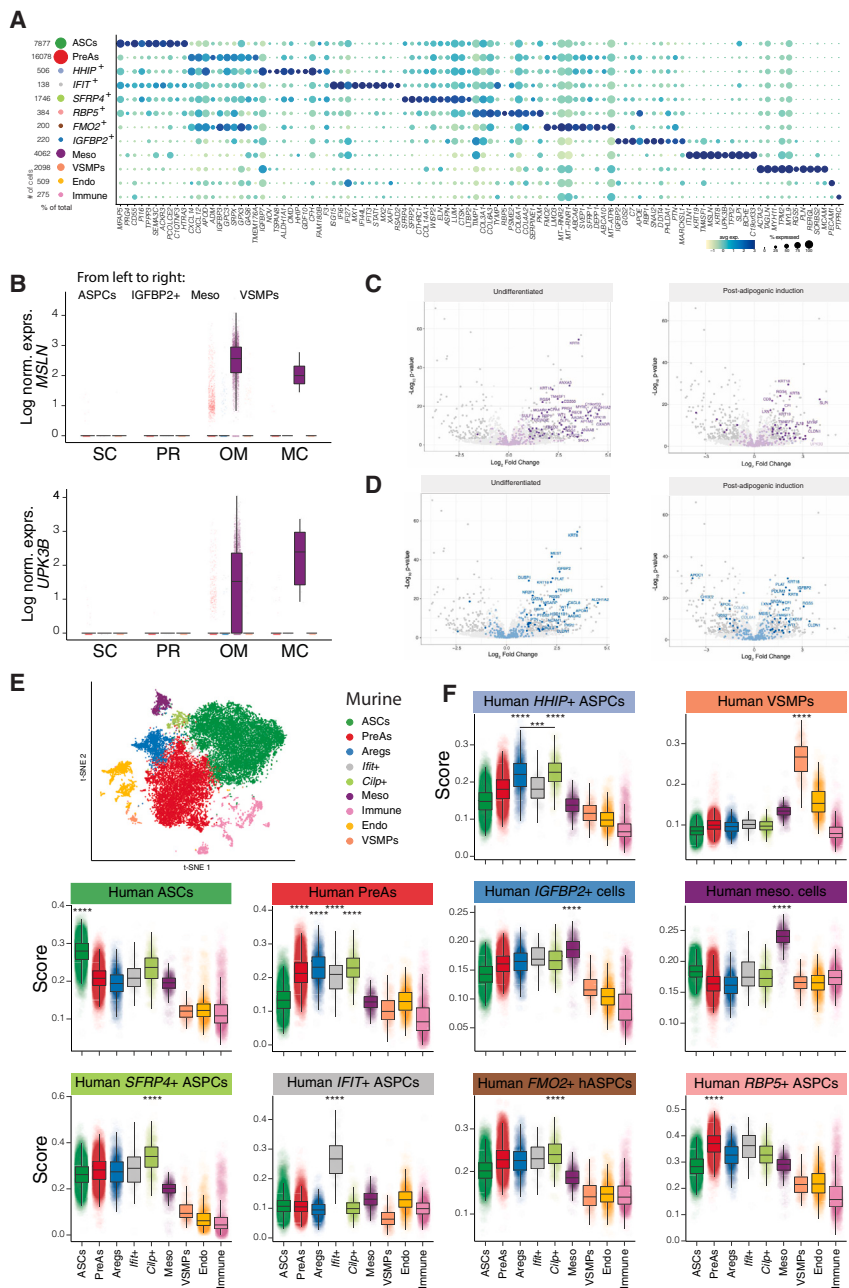
(C) t-SNE of the data in (B) colored by the identified cell cluster. The percentage of cells belonging to each cluster and the exact number of cells are shown on the right.

(D) Percentage per depot of cells in each cluster shown in (C) (excluding immune and endothelial cells).

(E) Log-normalized gene expression of selected markers in the different subpopulations depicted in (C). The boxplots display the mean as a dark band, the box shows the 25th and 75th percentiles, while the whiskers indicate the minimum and maximum data points.

(F) Heatmap of the differentially expressed genes between the human adipose stem cell (hASC) and the pre-adipocyte (hPreA) populations across depots, based on (C).

(G) UMAP of hASPCs and human mesothelial cells from the scRNA-seq data in Emont et al.⁵ colored by cell type/state when transferring our cell cluster annotation.



Common and unique stromal populations exist across adipose depots

In addition to hASCs and hPreAs, we identified five other depot-ubiquitous clusters (vascular smooth muscle progenitor [VSMC] cells, as well as HHIP+, IFIT+, SFRP4+, and RBP5+ cell populations), next to one PR and MC-specific (FMO2+) and two OM-specific (mesothelial and IGFBP2+) clusters (Figures 2C and 2D).

The VSMC population was identified based on the expression of muscle-related markers such as MYH11, ACTA2, and TAGLN (Figures 2E and 3A), resembling previously described signatures.²³

The HHIP+ cluster displayed several ortholog markers (F3, CLEC11A, GDF10, MGP, and INMT) of a mouse stromal

Figure 3. Common and unique stromal populations exist across adipose depots

(A) Dot plot of 10 differentially expressed markers for each cluster in Figure 2C.

(B) Log normalized expression of MSLN (top) and UPK3B (bottom) across hASCs, grouped by the depot of origin. The boxplots display the mean as a dark band, the box shows the 25th and 75th percentiles, while the whiskers indicate the minimum and maximum data points.

(C) Volcano plots displaying differential gene expression of SVF-adherent cells from the OM versus SC, PR, and MC. The top mesothelial markers identified using scRNA-seq datasets are dark purple, while differentially expressed genes ($\log_2FC > 1$, adjusted p value < 0.01) are light purple. Left: uninduced cells, right: differentiated cells.

(D) Volcano plots displaying differential gene expression of expanded SVF-adherent cells from the OM versus those from other depots (SC, PR, and MC). The top IGFBP2+ cell markers identified using scRNA-seq datasets are dark blue, while differentially expressed genes ($\log_2FC > 1$, adjusted p value < 0.01) are light blue. Left: uninduced cells, right: differentiated cells.

(E) t-SNE of integrated scRNA-seq datasets^{4,7,11} from mouse visceral and SC adipose depots, depicting the identified clusters.

(F) Boxplots—designed as in (B)—showing for each human cell population identified in Figure 2C the score of orthologous murine markers in each mouse cell population, as defined in Ferrero et al.⁹

subpopulation that we have previously characterized as Aregs^{7,12} (Figures 3A and S3A) and transcriptomically resembled the EPHA3+ cluster in the published human AT atlas.⁵ In our dataset, EPHA3 is specifically expressed by the HHIP+ cells (Figure S3A). Additionally, by transferring our annotation onto a published atlas,⁵ we confirmed that the EPHA3+ population has a significantly higher prediction score for our HHIP+ population than the rest of the hASCs (Figure S3B). Finally, given that HHIP is coding for a surface marker, we could confirm the existence of a human SVF

Lin[−]/HHIP+ cell population in the SC AT using flow cytometry (Figures S3C and S3D).

Another stromal population, the IFIT+ cluster, present in every depot and donor, is defined by the specific expression of interferon-related genes such as IFIT3, IFI6, and IFI27 (Figures 3A and S3E), reflective of a viral immune response (Figure S3F). Although a mesothelial Ifit+ population was reported in mouse OM,¹⁰ our IFIT+ population does not express mesothelial markers but mesenchymal ones (Figures 3A and S3G).

The SFRP4+ cluster was characterized by high expression of secreted frizzled-related proteins 2 and 4 (SFRP2 and SFRP4) (Figures 3A and S3H) and aligned with a subpopulation of the published human AT atlas⁵ (Figure S3I). Although SFRP4+

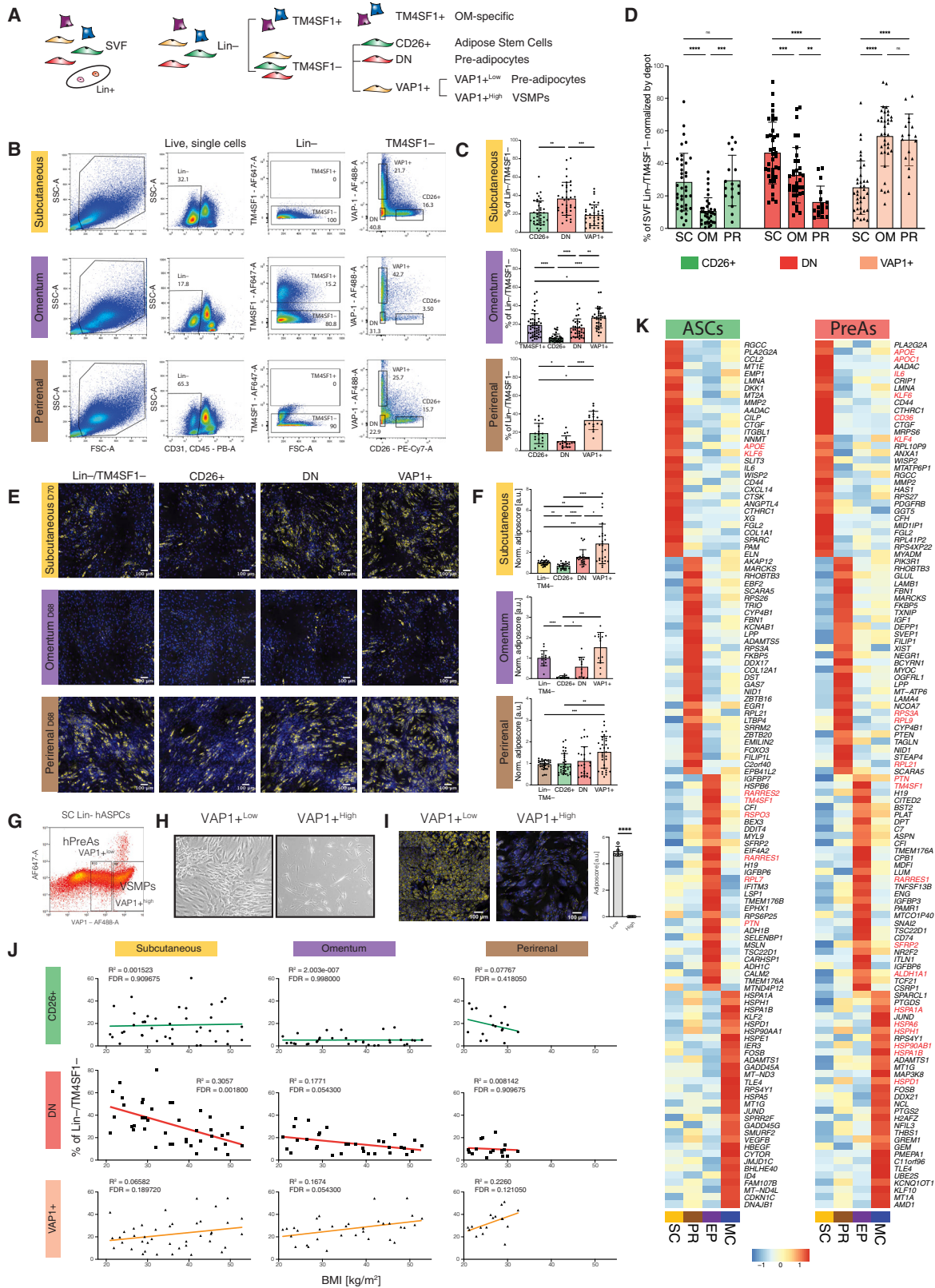


Figure 4. Exploring phenotypic differences among hASCs, hPreAs, and VSMPs

(A) Sorting strategy used to enrich for different hASC subpopulations and OM-specific cells.

(B) Flow cytometry profiles and gating strategy for SC, OM, and PR SVFs from the same donor to isolate SVF Lin⁻/TM4SF1⁻ cells.

(legend continued on next page)

hASPCs were present in all depots, we observed a higher expression of *SFRP2*, but not *SFRP4*, in hASPCs from OM adipose depots (Figures S3J and S3K).

We also found three depot-specific cell clusters: the *FMO2*+ hASPCs were specific to PR and MC, while the *IGFBP2*+ and mesothelial cells were mostly specific to the OM AT, albeit a few cells were also detected in MC (Figures 2C, 2D, and 3B), likely due to the MC being also covered by the peritoneum. The mesothelial cells, defined by the expression of *MSLN*, *UP3KB*, *LRRN4*, and keratin-related genes (Figures 3A–3C), constituted an abundant cell type in the OM AT (Figures 2A and 2D), consistent with the increased expression of keratin-related genes observed in bulk transcriptomics (Figure 3C). Similarly, *IGFBP2*+ cell markers, including *IGFBP2*, but also others such as *APOE* and *C7* (Figures 3A and 3C), were enriched in OM samples compared with other depots. Projecting our annotation onto the published human AT atlas⁵ validated the existence of a similar cell population in an independent dataset (Figures 2G and S2G).

Finally, we systematically mapped each cluster expression score computed on the integrated human scRNA-seq dataset onto the clusters that we have previously identified in mouse⁹ (Figures 3E and 3F) and found a high concordance between the proposed nomenclatures. This was further supported by flipping the analysis and mapping murine cluster expression scores onto the human-integrated dataset (Figure S3L).

In conclusion, our cross-anatomical analysis of human AT-derived stromal cells at the single-cell level revealed five populations that are present in all analyzed depots: the two canonical hASPC subpopulations (hASCs and hPreAs), VSMPs, and three less abundant stromal populations: *HHIP*+, *IFIT*+, and *SFRP4*+ cells. Specific to the OM SVF were the highly abundant mesothelial cell population and a less abundant *IGFBP2*+ cell cluster. Furthermore, we found high scRNA-seq cluster concordance between human and mice.

Isolation and phenotypic characterization of SVF Lin[−] subpopulations

We next aimed to functionally characterize the cellular subpopulations across depots. First, we focused on the two main populations: the hASCs and the hPreAs (Figure 2C). Based on our scRNA-seq expression data, we developed a sorting strategy (Figures 4A and 4B) in which hASCs were isolated as Lin[−]/TM4SF1[−]/CD26⁺ (referred to from here on as CD26+), given

the specific expression of *DPP4* (encoding for CD26; Figure S4A). The selection against the transmembrane 4 L6 family member 1 (TM4SF1) thereby aimed to deplete hASPCs from mesothelial and *IGFBP2*+ cells, present mostly in OM AT (Figures S4A–S4C). To isolate hPreAs, we focused on differentially expressed hPreA markers such as *GPC3* (Figure 2F), but the tested antibody showed poor performance on flow cytometry (data not shown). We therefore sorted hPreAs as Lin[−]/TM4SF1[−]/VAP1⁺ (referred to as VAP1+) based on the high expression of the vascular-adhesion protein 1 (VAP1), encoded by the *AOC3* gene, in the hPreA population (Figure S4A). This strategy, however, comes with the caveat that VAP1 is also highly expressed in VSMPs and that some hPreAs populations do not express VAP1 (Figures S4A and S4B). We therefore implemented an additional sorting layer aimed to enrich for the hPreAs that neither express CD26 nor VAP1 (Lin[−]/TM4SF1[−]/CD26[−]/VAP1[−], labeled as double-negative [DN] cells).

Using this sorting strategy, we analyzed the profiles of the Lin[−] portion of SVFs of 37 human donors (Table S1; Figure 4C). We found that the CD26+ pool is less abundant in OM AT compared with PR and SC ATs, while SC AT is dominated by DN cells and the OM and PR ones by VAP1+ cells (Figure 4D). The same three populations could be detected in the MC AT from two donors with ratios resembling those of OM AT (Figures S4D and S4E). Consistent with our transcriptomic findings, only the OM-derived SVF showed a clearly positive TM4SF1 population (Figures 4B, 4C, and S4F), albeit a few TM4SF1+ cells were also detected in MC SVF Lin[−] (Figure S4F).

Having confirmed the existence of these subpopulations, we next aimed to interrogate their phenotypic behavior *in vitro*. When sorted separately, the CD26+ population proliferated faster than all other populations, regardless of the depot of origin (Figure S4G). CD26+ cells also scored the lowest in terms of adipogenic potential (Figures 4E and 4F), supporting that they are located at the root of the adipogenic lineage.⁴ The VAP1+ cells had the highest adipogenic potential, followed by DN cells (Figures 4E and 4F). However, as mentioned above, VAP1+ cells likely included both hPreAs and VSMPs. Hence, we aimed to clarify which populations were responsible for this high adipogenic potential. Since *AOC3* expression was higher in VSMPs than PreAs in the scRNA-seq data (Figure S4A), we stratified the VAP1+ population into cells with mild (VAP1+^{low}; excluding the top ~20% positive cells) or high VAP1 expression (VAP1+^{high};

(C) Abundance of each cell subpopulation gated from the Lin[−]/TM4SF1[−] fraction of SVF cells; SC *n* = 37, OM *n* = 35, PR *n* = 17 donors.

(D) Relative proportion of the indicated SVF populations across depots; SC *n* = 37, OM *n* = 35, PR *n* = 17 donors.

(E) Representative fluorescence microscopy images of SVF Lin[−]/TM4SF1[−], CD26+, DN, and VAP1+ populations from each depot after adipogenic differentiation; yellow, lipids; blue, DNA; scale bars, 100 μm.

(F) Adiposcores quantified from fluorescence microscopy as in (E). Values are normalized to the average adiposcore of the Lin[−]/TM4SF1[−] population; *n* = 12–21, 3–7 donors, 1–4 independent wells each.

(G) Flow cytometry profiles of SC Lin[−] cells, showing the gating strategy to isolate VAP1+^{low} hPreAs and VAP1+^{high} VSMPs; *n* = 3.

(H) Bright-field microscopy images of expanding VAP1+^{low} hPreAs and VAP1+^{high} VSMPs.

(I) Representative fluorescence microscopy images of differentiated VAP1+^{low} hPreAs and VAP1+^{high} VSMPs and adiposcore quantification from *n* = 5, 3 donors, 1–2 wells per donor.

(J) Correlation between the % Lin[−]/TM4SF1[−] cells from each indicated SVF population and BMI across donors.

(K) Heatmap of the top 30 higher expressed genes in the indicated depot versus all other depots, focusing on hASCs (left) or hPreAs (right). Average log normalized expression scaled by row.

p* ≤ 0.05, *p* ≤ 0.01, ****p* ≤ 0.001, *****p* ≤ 0.0001, one-way ANOVA and Tukey HSD post hoc test (C, D, F, and I), and linear regression analysis with its relative goodness of fit and the false discovery rate (FDR)-adjusted *p* values of the Pearson correlations (G). All bar plots display the mean value and the standard deviation from the mean as error bar.

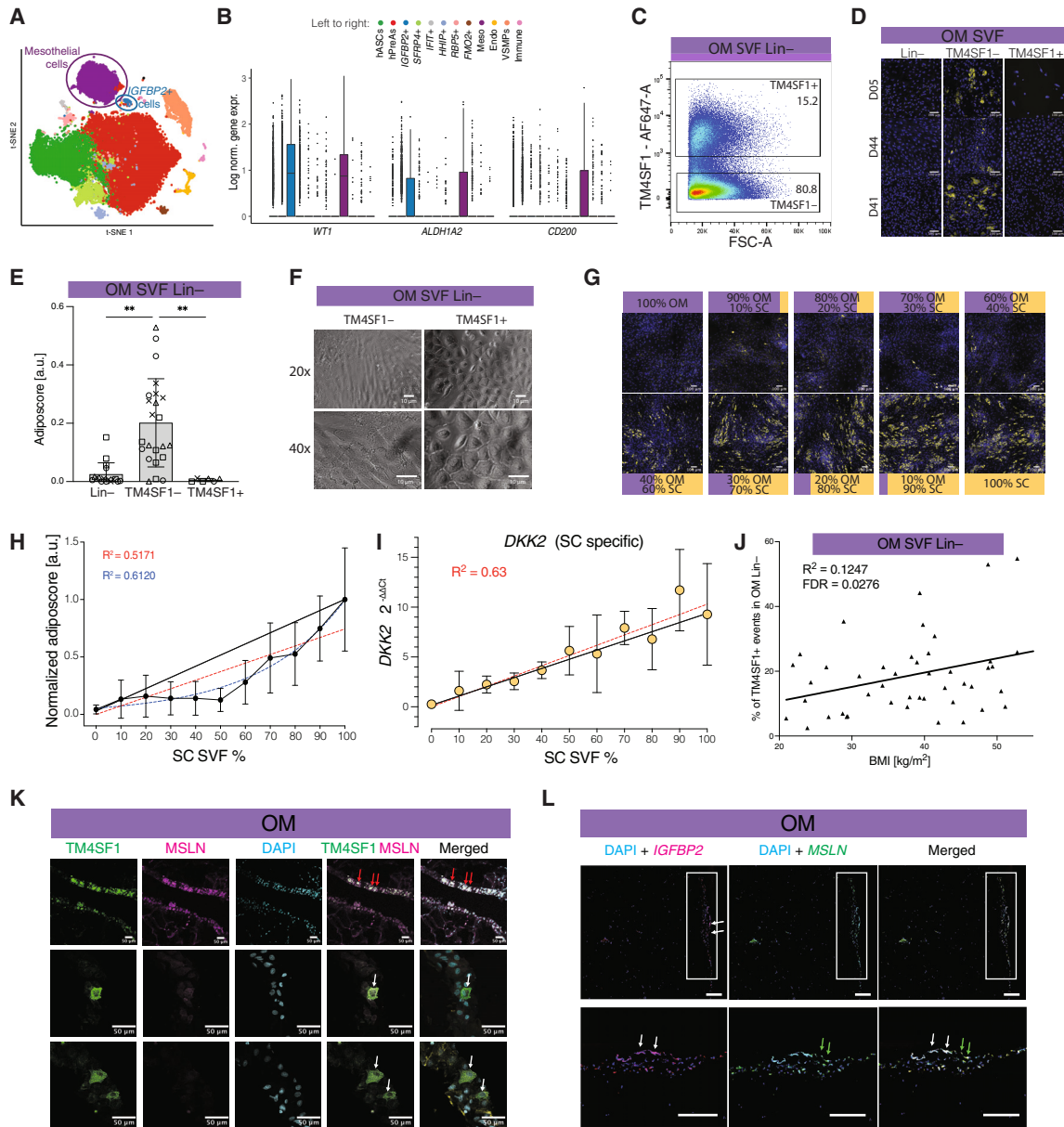


Figure 5. OM-specific cells inhibit adipogenesis of hASPCs

(A) t-SNE of integrated scRNA-seq datasets highlighting the mesothelial and *IGFBP2*+ populations.

(B) Log-normalized expression of *WT1*, *ALDH1A2*, and *CD200* across the indicated cell populations, based on the scRNA-seq data in (A). The boxplots display the mean as a dark band, the box shows the 25th and 75th percentiles, while the whiskers indicate the minimum and maximum data points in the considered dataset.

(C) Flow cytometry gating strategy for sorting OM SVF Lin⁻-specific subpopulations as Lin⁻/TM4SF1⁺ and Lin⁻/TM4SF1⁻ cells.

(D) Representative fluorescence microscopy images of OM SVF Lin⁻, Lin⁻/TM4SF1⁻, and Lin⁻/TM4SF1⁺ cells after differentiation.

(E) Adiposcore quantification of the cell populations shown in (D); *n* = 6–23, 4 donors, 1–6 independent wells for each. The bar plots display the mean value and the standard deviation from the mean as error bar.

(F) Bright-field microscopy images of spindle-like OM hASPCs (Lin⁻/TM4SF1⁻) and cobblestone-like TM4SF1⁺ populations.

(G) Representative fluorescence microscopy images of SVF Lin⁻ cells in mixing experiments after 14 days of differentiation. SVF Lin⁻ cells from OM and SC adipose tissues (ATs) were mixed directly after isolation at the indicated proportions.

(H) Adiposcore quantification of the distinct, mixed OM and SC SVF Lin⁻ cell populations shown in (G). Values are normalized to the adiposcore of the 100% SC Lin⁻ condition. Error bars represent standard deviation from the average; the linear and exponential regression with corresponding *R*² coefficients are shown in red and blue, respectively. The black line represents the expected increase of adipogenesis for a linear dilution between 0% and 100% of SC SVF Lin⁻ cells; *n* = 16, 4 biological replicates, 4 independent wells for each.

(I) Gene expression levels of *DKK2* (a SC-specific gene), normalized by *HPRT1* expression and 0% SC to control for correct mixing ratios in (G). Error bars represent standard deviation from the average. The linear regression and corresponding *R*² coefficient values are shown in red; a black line links the lowest value to the highest value; *n* = 4, 2 biological replicates, 2 independent wells for each.

(legend continued on next page)

top ~15% positive cells) (Figure 4G). Upon plating, VAP1^{high} cells adopted the long spindle shape characteristic of VSMPs (Figure 4H) and failed to differentiate into adipocytes (Figure 4I). By contrast, VAP1^{low} cells showed a classic mesenchymal appearance and a remarkable adipogenic differentiation capacity (Figures 4H and 4I), consistent with being a hPreA-enriched fraction. Therefore, the high adipogenic capacity of the VAP1⁺ fraction is likely driven by VAP1^{low}/hPreAs and not by VAP1^{high}/VSMPs.

We then investigated potential correlations between the relative abundance of each of the SVF Lin[−] subpopulations and metadata such as BMI, age, and sex of the donors for each depot. Interestingly, we found that although the proportion of CD26⁺ cells is not affected by BMI, the latter appears to be correlated with DN cell depletion. This anti-correlation is particularly high in the SC but also in the OM AT and is accompanied by a slight increase in the proportion of VAP1⁺ cells (Figure 4J). By contrast, the age or sex of the donor did not seem to affect the equilibrium of cell populations within the SVF Lin[−] pool of any of the analyzed depots (data not shown).

All three OM populations were consistently and significantly less adipogenic than equivalent SC and PR cells (Figure 4E). To determine if cell-intrinsic features could explain the different adipogenic potential, we explored the depot-specific transcriptomic signatures of these subpopulations in our scRNA-seq dataset. We noticed that across depots, the transcriptomes of hASC cells are more similar than the hPreA ones (Figures 2F and S4H), supporting the hypothesis that depot-specific features accumulate along commitment. We then identified genes of hASCs or hPreAs enriched in a depot-specific manner (Figure 4K). In line with their high adipogenic potential, hASCs and hPreAs from SC and PR depots showed significantly higher expression of well-known adipogenic genes and transcription factors, such as *KLF4*, *KLF6*, *WISP2*, *APOE*, *APOC1*, and *CD36* (Figure S4I). For example, *PIK3R1* is the most up-regulated gene in PR compared with other adipose depots, with phosphatidylinositol 3-kinase (PI3K) signaling playing a crucial role in adipogenesis of human mesenchymal stem cells.²⁴ With respect to populations that showed limited adipogenic potential, MC cells overexpressed genes linked to unfolded protein or protein folding (Figure S4I), such as heat shock proteins (HSPs) (Figure 4K), a large family of molecular chaperones. HSPs have been reported to interact with the peroxisome proliferator-activated receptor γ (PPAR γ) to either stabilize it and enhance adipogenesis (Hsp90)²⁵ or to destabilize it and inhibit adipogenesis (Hsp20).²⁶ By contrast, OM cells once again showed an enrichment of genes linked to the inflammatory response (Figure S4I) as well as a number of markers previously described to negatively impact adipogenesis (*RARRES2*, *RSPO3*, *RPL7*, *PTN*, *GAL*, *ALDH1A1*, and *IGFBP3*^{17,27–29}; Figure 4K).

Taken together, we showed that the hASPC niche harbors different subpopulation abundances depending on the anatomic

origin, and its equilibrium changes with increasing BMI. Furthermore, even if ubiquitous across depots, hASCs and hPreAs display depot-specific gene signatures, seemingly acquired along commitment.

OM-specific cells inhibit the adipogenesis of omental and s.c. hASPCs

We next wondered if the presence of OM-specific cell populations (e.g., mesothelial and *IGFBP2*⁺ cells; Figure 5A) might influence the adipogenic capacity of SVF cells from this depot, as these unique subpopulations expressed several genes previously linked to the adipogenic impairment of omental SVF cells (e.g., *CD200*, *WT1*, and *ALDH1A2*,^{17,30} Figure 5B).

Using TM4SF1 as a surface marker for the two OM-specific populations (Figure S4C), we studied the adipogenic potential of OM hASPCs with or without TM4SF1⁺ cells (Figure 5C). We confirmed that OM Lin[−]/TM4SF1[−] cells (now referred to as OM hASPCs) are significantly more adipogenic than the total OM Lin[−] fraction (Figures 5D and 5E). By contrast, OM Lin[−]/TM4SF1⁺ cells (TM4SF1⁺) did not accumulate LDs and showed the round cobblestone-like shape characteristic of mesothelial cells³¹ (Figures 5D–5F). Importantly, the increase in differentiation observed for OM hASPCs cells compared with the whole Lin[−] fraction was greater than that expected from the proportional removal of TM4SF1⁺ cells (accounting for roughly 20% of the total Lin[−] fraction, Figure 4C). This suggests that TM4SF1⁺ cells might repress the adipogenic capacity of OM hASPCs.

To assess the inhibitory effect of OM-specific cells on differentiation, we co-cultured typically highly adipogenic SC or PR Lin[−] cells with an increasing ratio of OM Lin[−] cells (Figures 5G and 5H for SC and S5A and S5B for PR). The adipogenic potential of the co-culture was not linear to the proportion of OM to SC Lin[−] cells (Figure 5H). However, the expression of *DKK2*, a SC-specific marker (Figure S5C), linearly increased with the proportion of SC cells, ruling out the possibility that SC cells were overgrown by OM cells (Figure 5I). Mixing OM Lin[−] cells with PR Lin[−] ones showed no discernible regulatory effect, as evidenced by a relatively linear relationship between the increase in differentiation and the proportion of PR cells (Figures S5A and S5B). Thus, our findings suggest that OM TM4SF1⁺ cells lower the adipogenic capacity of neighboring cells and that the sensitivity to this inhibition is depot-specific. This ability of OM TM4SF1⁺ cells to inhibit adipogenesis suggests a possible role of this subpopulation in OM AT expansion. Interestingly, the relative fraction of OM TM4SF1⁺ cells within the total SVF Lin[−] cell pool positively correlated with the BMI of donors (Figure 5J).

Based on our scRNA-seq data, TM4SF1⁺ OM-specific cells could be further stratified into two populations: the classic mesothelial cells and the *IGFBP2*⁺ cluster (Figure 5A). To study these populations separately, we used TM4SF1 as a marker to enrich both OM-specific populations and added mesothelin

(J) Correlation between the OM SVF/Lin[−]/TM4SF1⁺ fraction based on flow cytometry analysis and the BMI of donors; the line represents a linear regression analysis with its relative goodness of fit; the *p* value was computed performing a Pearson correlation.

(K) Immunohistochemistry-based localization of TM4SF1⁺ (green) and MSLN⁺ (pink) cells in OM AT. The arrows indicate TM4SF1⁺/MSLN[−] cells (white) and TM4SF1⁺/MSLN⁺ cells (red) in the periphery of the AT lobules. Scale bars, 50 μ m.

(L) RNAScope *in situ* localization of *IGFBP2*⁺ (pink) and MSLN⁺ (green) cells in OM AT. The arrows indicate *IGFBP2*⁺/MSLN⁺ cells (white) and *IGFBP2*[−]/MSLN⁺ cells (green) in the periphery of the AT lobules. Scale bars, 200 μ m.

For (D) and (G): yellow, lipids; blue, DNA; scale bars, 100 μ m. For (K) and (L): cyan, DNA.

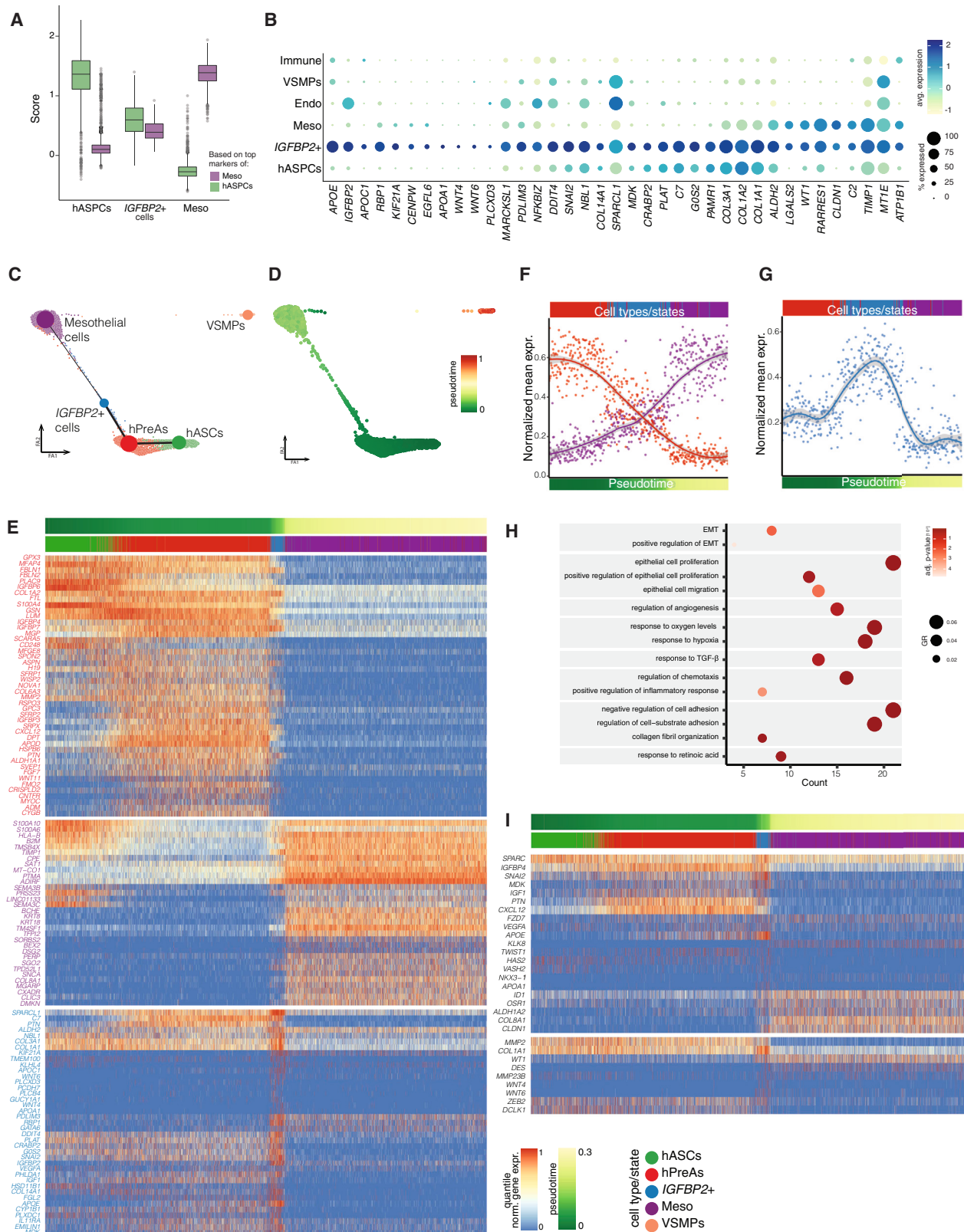


Figure 6. IGFBP2+ cells could transition between mesothelial and mesenchymal states

(A) Score distribution based on the top mesothelial markers or hASPC markers in OM hASPCs, IGFBP2+ cells, and mesothelial cells. The boxplots display the mean as a dark band, the box shows the 25th and 75th percentiles, while the whiskers indicate the minimum and maximum data points in the considered dataset.

(legend continued on next page)

(MSLN) as a classic marker to enrich specifically for mesothelial cells, as *MSLN* expression is higher in mesothelial compared to *IGFBP2*⁺ cells (Figures S4A and S4C). We therefore defined mesothelial cells as TM4SF1+/MSLN^{high} and *IGFBP2*⁺ cells as TM4SF1+/MSLN^{low}. To validate the presence of these two populations *in vivo*, we first performed immunohistochemistry analyses using antibodies directed against both MSLN and TM4SF1, both of which highly stained the boundaries of the AT lobules (Figure S5D), revealing the mesothelial mono-layer peritoneum structure around the OM. Most positively stained cells were equally intense for both markers (Figures 5K and S5D, red arrows). However, some cells exhibited a disproportionately higher intensity in the TM4SF1 channel compared with the MSLN one (Figures 5K and S5D, white arrows), reminiscent of the gene expression characteristics of the *IGFBP2*⁺ cells. We next aimed to more directly visualize *IGFBP2*⁺ cells, but since *IGFBP2* is a secreted protein,^{32,33} immunohistochemistry may not be suitable. We therefore employed *in situ* hybridization using RNAScope technologies.³⁴ In line with the histology and scRNA-seq data, most *IGFBP2*-positive cells co-expressed *MSLN* to some degree (Figure 5L, white arrows). However, most *MSLN*-positive cells did not express *IGFBP2* (Figure 5L, green arrows). Hence, the scRNA-seq, immunohistochemistry, and RNAScope data show that classic mesothelial cells can be differentiated from the *IGFBP2*⁺ cluster, even if the *IGFBP2*⁺ cells still residually express *MSLN*.

Omental *IGFBP2*⁺ stromal cells transition between mesothelial and mesenchymal states

Our scRNA-seq datasets unveiled that the *IGFBP2*⁺ cluster had an intriguing dual gene expression signature, sharing markers with both hASPCs and mesothelial cells (Figure 6A). Importantly, *IGFBP2*⁺ cells did not display a larger library size or number of captured features (Figure S6A), limiting the possibility of such cells being doublets. In addition, these cells express specific markers such as *IGFBP2*, *RBP1*, *WNT4*, or *WNT6* and also markers to a higher level than in hASPCs or mesothelial cells alone (Figure 6B), which is technically impossible for randomly co-encapsulated cells. When transferring our cell annotation onto the published human SC and OM AT single-cell atlas,⁵ we found that only cells from OM harbor a positive prediction score for *IGFBP2*⁺ cells (Figure S6B). Further, the cells predicted as *IGFBP2*⁺ cells aligned with a cluster that was independently identified in the AT single-cell RNA-seq atlas⁵ (Figures S2G

and S6C–S6E) and showed enrichment for *IGFBP2*⁺ cell markers (Figure S6E). Interestingly, the abundance of this population (relative to hASPCs and mesothelial cells) correlated with the BMI of the donors ($\rho = 0.95$, Figure S6F). Aside from expressing their own specific markers (Figures S6G and S6H), the predicted cells co-expressed mesothelial and hASPC markers (Figure S6I) and aligned along a “bridge” between the two cell types. This duality in gene expression could reflect cells that are transitioning from one cell type to another. To computationally test this hypothesis, we performed trajectory inference on our aggregated OM scRNA-seq datasets, using partition-based graph abstraction (PAGA).³⁵ The inferred graph predicted branches connecting OM hASPCs to mesothelial cells through *IGFBP2*⁺ cells (Figures 6C and 6D). As positive and negative controls of the validity of the graph structure, hASCs and hPreAs were connected by a robust branch, while VSMPs were not connected to the main trajectory. When ordering the cells by their pseudotime along the trajectory starting from hASCs to mesothelial cells (Figure 6E), we observed a gradual decrease and increase of hASPC and mesothelial cell markers, respectively, along the connecting branch (Figure 6F), as well as an up-regulation of *IGFBP2*⁺ cell markers (Figure 6G). Altogether, these results indicate that *IGFBP2*⁺ cells might represent cells that transition between mesothelial and mesenchymal cell types. Accordingly, we found the gene ontology (GO) term “epithelial-to-mesenchymal transition” (EMT) to be enriched in *IGFBP2*⁺ cells (Figure 6H), as well as a higher expression of genes from the Wnt family, matrix metalloproteinases (MMPs), zinc finger E-box binding (ZEB) transcription factors, and others previously linked with EMT^{36,37} (Figure 6I). Transforming growth factor β (TGF- β) signaling has also been described as a master regulator of EMT linked to wound healing and fibrosis.^{38,39} In line, we found that *IGFBP2*⁺ cells have an enriched expression linked to “response to TGF- β ” (Figure 6H). Other GO terms related to EMT, such as angiogenesis, hypoxia, inflammatory responses, cell cycle markers, and down-regulation of adhesion molecules,⁴⁰ were all significantly enriched among the *IGFBP2*⁺ cell markers (Figure 6H). Thus, our findings point to the existence of cells that likely transition between mesothelial and mesenchymal cell types.

Omental *IGFBP2*⁺ stromal cells inhibit adipogenesis through *IGFBP2*

To isolate and functionally characterize *IGFBP2*⁺ cells aside from mesothelial cells based on their underlying gene expression

(B) Average expression and percentage of expressing cells of the top *IGFBP2*⁺ cell markers across the clusters in Figure 2C.

(C) PAGA-inferred trajectory superimposed on ForceAtlas2 layout.³⁵ The size of the dots is proportional to the number of cells in the cluster, and the thickness of the lines is proportional to the confidence of the trajectory relationship.

(D) PAGA-inferred trajectory described in (C), colored by the inferred pseudotime (starting from hASCs).

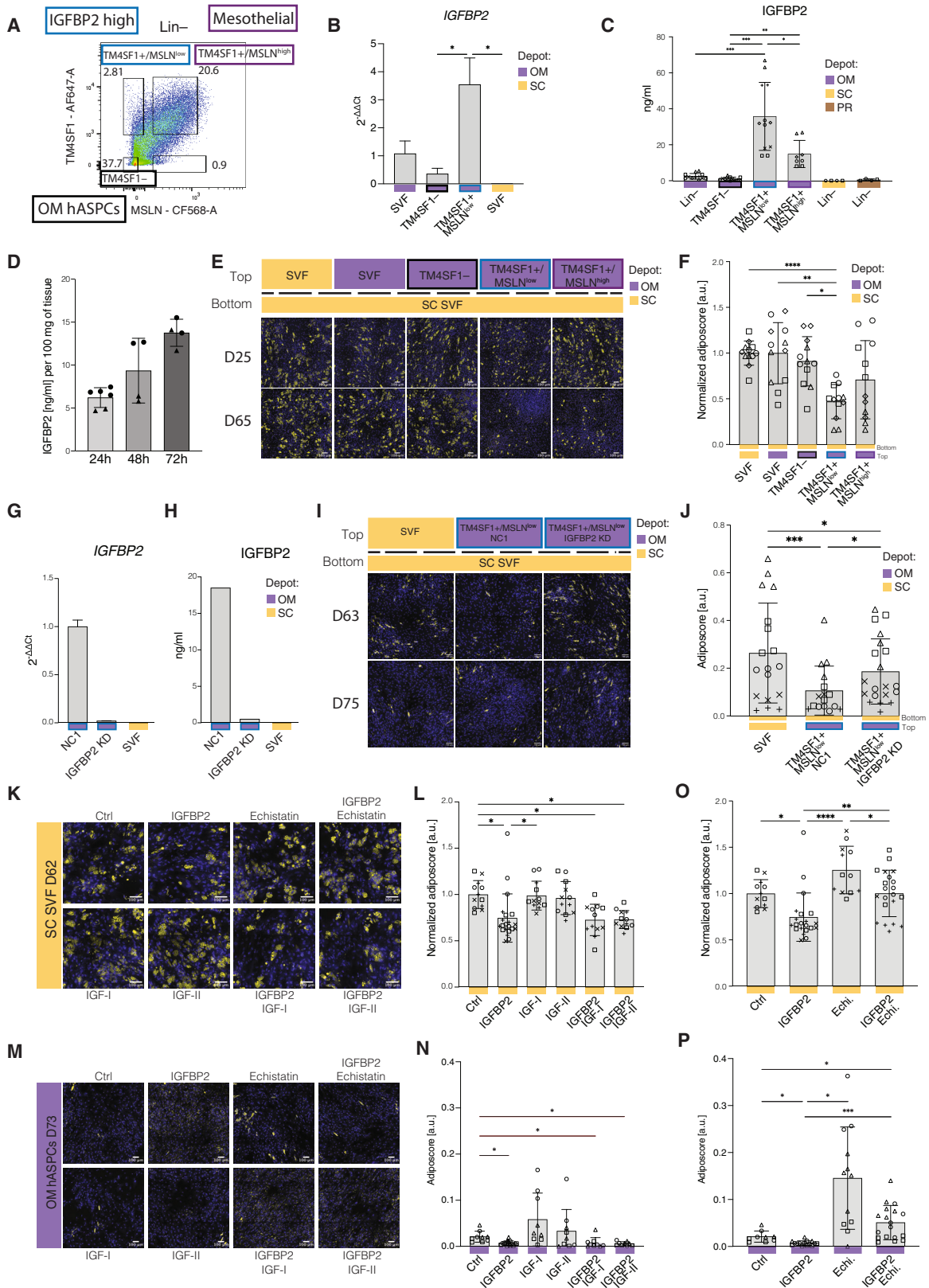
(E) Heatmap showing the gene expression changes along pseudotime calculated on the trajectory shown in (D). Red: genes decreasing from hASPCs to mesothelial cells; purple: genes increasing from hASPCs to mesothelial cells; blue: genes specific to *IGFBP2*⁺ cells; log-normalized gene expression scaled by row (quantile normalization).

(F) Average of quantile-normalized gene expression highlighted in red or purple in (E) for each cell along the pseudotime shown in (D). The plot focuses on the transition between hPreAs (red) and mesothelial cells (purple), passing by *IGFBP2*⁺ cells (blue). A locally estimated scatterplot (LOESS) smoothing with 95% confidence interval is shown.

(G) As in (F), but for the gene expression highlighted in blue, focusing on the transition between hPreAs (red) and mesothelial cells, passing by *IGFBP2*⁺ cells (blue).

(H) Dot plot of key GO terms enriched based on *IGFBP2*⁺ cell markers.

(I) Change in gene expression along the trajectory pseudotime shown in (D) for EMT-related genes (top: enriched genes when performing GO enrichment analysis, bottom: other EMT-related genes found in the literature).



(legend on next page)

signature (Figure S2C), we used fluorescence-activated cell sorting (FACS) to further segregate the Lin⁻/TM4SF1⁺ population based on MSLN signal. As such, mesothelial cells (Lin⁻/TM4SF1⁺/MSLN^{high}) were separated from low-MSLN-expressing *IGFBP2*⁺ cells (Lin⁻/TM4SF1⁺/MSLN^{low}). Additionally, remaining OM hASPCs could be collected as the Lin⁻/TM4SF1⁻ fraction (Figures 7A and S7A). This sorting strategy was validated by the higher *IGFBP2* expression in Lin⁻/TM4SF1⁺/MSLN^{low} cells compared with OM hASPCs (Lin⁻/TM4SF1⁻) and SC SVF Lin⁻ cells (Figure 7B). Interestingly, confluent Lin⁻/TM4SF1⁺/MSLN^{low} cells displayed the classic mesothelial-cobblestone-like morphology; however, when expanding, they tended to adopt a spindle-like shape, resembling mesenchymal cells (Figure S7B), supporting their potential transitioning state. Concordant with *IGFBP2* being a secreted factor,^{32,33} the concentration of *IGFBP2* in the supernatant of OM Lin⁻/TM4SF1⁺/MSLN^{low} cells was significantly higher than that of Lin⁻/TM4SF1⁺/MSLN^{high} cells, or that in the supernatant of OM, SC, or PR hASPCs (Figure 7C). We could also confirm that *IGFBP2* is secreted by OM AT incubated *ex vivo* and in a linear fashion over time (Figure 7D).

Since *IGFBP2* has been shown to have anti-adipogenic properties,^{32,41,42} we wondered whether *IGFBP2*-expressing cells could account for the paracrine anti-adipogenic effects of the OM TM4SF1⁺ fraction (Figures 5D and 5E). To test this, we used a transwell setup where we seeded adipogenic SC SVF Lin⁻ cells at the bottom and different fractions of OM stromal cells at the top (Figure 7E). We observed that OM Lin⁻/TM4SF1⁺/MSLN^{low} cells exerted the strongest adipogenic inhibition on SC cells, while a much milder inhibition was observed when SC cells were exposed to the OM Lin⁻/TM4SF1⁺/MSLN^{high} fraction (Figures 7E

and 7F). In agreement with the co-culture experiments (Figures S5A and S5B), PR hASPCs were refractory to the anti-adipogenic action of OM SVF Lin⁻ cell subpopulations in the transwell setting (Figures S7C and S7D).

To assess whether *IGFBP2* secretion accounted for the anti-adipogenic effects of *IGFBP2*-expressing cells, we knocked down (KD) *IGFBP2* using small interfering RNA (siRNA). After validating the KD both at the mRNA and secreted protein levels (Figures 7G and 7H), we used again a transwell setup to expose SC SVF Lin⁻ cells to cells transfected with either control (NC1) or *IGFBP2* siRNAs. The SC cells exposed to the *IGFBP2* KD cells formed significantly more LDs than those exposed to the control-transfected cells (Figures 7I and 7J), supporting that *IGFBP2* secretion participates in the anti-adipogenic actions of Lin⁻/TM4SF1⁺/MSLN^{low} cells. In agreement, the treatment with exogenous recombinant *IGFBP2* was enough to inhibit adipogenesis in SVF cells from SC or PR depots in a dose-dependent manner starting from 2 nM, even if the effect was milder in PR cells (Figures 7K–7O, S7E, and S7F). This concentration falls in a similar range (1 nM = 33 ng/mL) as that measured in the supernatant of *IGFBP2*⁺ cells (Figure 7C).

IGFBP2 inhibits adipogenic differentiation through integrin signaling

IGFBP2 can act through either insulin-like growth factor (IGF)-dependent or IGF-independent pathways.⁴³ In the first scenario, the presence of *IGFBP2* in the extracellular environment of hASPCs would sequester IGF-I and/or IGF-II and interfere with their pro-adipogenic signaling.^{44–47} To test whether *IGFBP2* acts by sequestering IGFs, we co-treated SVF-adherent cells

Figure 7. Omental *IGFBP2*⁺ stromal cells inhibit adipogenesis through *IGFBP2*

- (A) Flow cytometry gating strategy to enrich for specific OM SVF Lin⁻ subpopulations: Lin⁻/TM4SF1⁻ (OM ASPCs), Lin⁻/TM4SF1⁺/MSLN^{low} (*IGFBP2*⁺ cells), or Lin⁻/TM4SF1⁺/MSLN^{high} (mesothelial cells).
- (B) *IGFBP2* expression in OM SVF cell subpopulations; *n* = 4, 2 donors, 2 replicates.
- (C) *IGFBP2* secretion by the indicated populations during 48 h; *n* = 8, 4 donors, 2 replicates.
- (D) *IGFBP2* secretion by 100 mg of OM adipose tissue over the indicated time window; *n* = 4, 2 donors, 2 replicates.
- (E) Representative fluorescence microscopy images of SC SVF cells at the bottom of a transwell setup, after adipogenic differentiation when co-cultured with the indicated populations on top of the transwell.
- (F) Adiposcore quantification of “receiver” cells as shown in (E). Values are normalized to the average adiposcore of the reference top SC SVF-adherent condition; *n* = 12, 4 donors, 3 independent wells.
- (G) *IGFBP2* expression in SVF/Lin⁻/TM4SF1⁺/MSLN^{low} cells subjected to *IGFBP2* siRNA (*IGFBP2* KD) or non-targeting siRNA control (NC1). SC SVF-adherent cells were used as negative control; *n* = 2, 1 donor, two technical replicates.
- (H) *IGFBP2* levels in the supernatant of OM SVF Lin⁻/TM4SF1⁺/MSLN^{low} cells subjected to *IGFBP2* siRNA (*IGFBP2* KD) or non-targeting siRNA control (NC1). SC SVF/Lin⁻ cells were used as negative control; *n* = 2, 1 donor, two technical replicates.
- (I) Representative fluorescence microscopy images of SC SVF cells at the bottom of the transwell setup after adipogenic differentiation when co-cultured with the indicated cells on top of the transwell.
- (J) Adiposcore quantification of receiver cells as shown in (I); *n* = 16–20, 4 donors, 2–4 independent wells.
- (K) Representative fluorescence microscopy images of SC SVF cells after adipogenic differentiation when treated with: *IGFBP2* 2 nM, IGF-I 10 nM, IGF-II 10 nM, and echistatin 100 nM.
- (L) Adiposcore quantification of cells as shown in (K), focusing on the IGF-dependent signaling pathway of *IGFBP2*. Values are normalized to control cells (Ctrl); *n* = 12, 4 donors, three independent wells.
- (M) Representative fluorescence microscopy images of OM hASPCs after adipogenic differentiation when treated as in (K).
- (N) Adiposcore quantification of cells as shown in (M), focusing on the IGF-related signaling pathway. Values are normalized to control cells (Ctrl); *n* = 9, 3 donors, three independent wells.
- (O) Adiposcore quantification of cells as shown in (K), focusing on the integrin-related signaling pathway. Values are normalized to control cells (Ctrl); *n* = 12, 4 donors, three independent wells.
- (P) Adiposcore quantification of cells as shown in (M), focusing on the integrin-related signaling pathway. Values are normalized to control cells (Ctrl); *n* = 9, 3 donors, three independent wells.

For (E), (I), (K), and (M): yellow, lipids; blue, DNA; scale bars, 100 μm. **p* ≤ 0.05, ***p* ≤ 0.01, ****p* ≤ 0.001, *****p* ≤ 0.0001, one-way ANOVA and Tukey HSD post hoc test (B, C, F, L, and O), REML analysis with matched values for the same donor, and Tukey HSD post hoc test (J, N, and P). All bar plots display the mean value and the standard deviation from the mean as error bar.

with both IGFBP2 and IGF-I or IGF-II, as well as with the three recombinant proteins alone. Although most literature uses IGF-I and IGF-II at concentrations around 10 nM,^{45–47} we were unable to observe a significant effect on the adipogenic potential of hASPCs at any concentration ranging from 2.5 to 40 nM (Figures S7E and S7F). However, our adipogenic cocktail typically induces high lipid accumulation, which could be masking any adipogenic effect of IGFs. To control for this, we also tested the effects of IGFs with less potent adipogenic cocktails. Yet, in none of them, IGF-I or IGF-II influenced lipid accumulation (Figure S7G). Moreover, for SC cells, the inhibitory effect of IGFBP2 on adipogenesis was comparable in the presence or in the absence of IGFs (Figures 7K–7L), suggesting that IGFBP2 influences adipogenesis in an IGF-independent manner. Once again, PR lines appeared to be less sensitive to the action of IGFBP2 and IGF treatments (Figures S7J and S7K), which is consistent with our previous observations suggesting that PR SVF-adherent cells are less sensitive to the inhibitory effect of OM SVF Lin[−] cells or OM SVF Lin[−]/TM4SF1+/MSLN^{low} cells in the transwell setup (Figures S5A, S5B, S7C, and S7D).

Next, we explored to what extent OM hASPCs can themselves respond to IGFBP2 and IGF treatments since these cells anatomically co-localize with the IGFBP2-secreting cells. Even if OM TM4SF1[−] cells are intrinsically lowly adipogenic, we observed an impaired differentiation capacity when these cells were treated with IGFBP2 (Figures 7M and 7N). Contrary to PR and SC cells, OM cells were more sensitive to the IGF-I and IGF-II treatments but with a high degree of variability between batches (Figures 7M and 7N). However, when co-treated with IGFs and IGFBP2, the differentiation of OM TM4SF1[−] cells was again significantly lower than in non-treated cells (Figures 7M and 7N). The fact that IGF treatment did not influence the actions of IGFBP2 strengthens the concept of an IGF-independent mode of action by IGFBP2.

Alternatively, IGFBP2 can also bind integrin receptors recognizing RGD domains, most notably the $\alpha 5\beta 1$ integrin receptor, whose signals can preclude adipocyte differentiation.⁴⁸ To test the influence of integrin receptor signaling in the anti-adipogenic actions of IGFBP2, we used echistatin, a known antagonist of RGD-binding integrin receptors.⁴⁹ When cells were co-treated with IGFBP2 and echistatin, the adipogenic potential of the treated cells was similar to that of non-treated control cells (Figures 7K and 7O). The engagement of integrin signaling by IGFBP2 was confirmed by analyzing the phosphorylation of the extracellular-signal-regulated kinases 1 and 2 (ERK1/2), which are activated in response to RGD-binding integrin receptors.^{50–53} IGFBP2 increased the phosphorylation of ERK1/2 in SVF cells from SC AT, and this action was abrogated by echistatin treatment (Figure S7H). By contrast, ERK1/2 activation by insulin was unaffected by echistatin, supporting the specific effect on IGFBP2 signaling (Figure S7H). Interestingly, IGFBP2 also triggered ERK1/2 signaling in PR AT, yet to a more modest degree (Figure S7I), which could explain why IGFBP2 treatment at this concentration did not significantly repress adipogenesis. Our results also indicated that echistatin treatment significantly enhances the differentiation of SC SVF-adherent cells (Figures 7K and 7O), while yielding a milder yet significant increase in overall adipogenic potential in PR cells compared with SC cells (Figures S7J and S7L). This suggests that the IGFBP2/in-

tegrin signaling axis is more prominent in SC AT. Most strikingly, when treating OM TM4SF1[−] cells with echistatin, we observed a significant increase in the ability of these intrinsically non-adipogenic cells to accumulate LDs (Figures 7M and 7P). Furthermore, co-treatment with echistatin and IGFBP2 led to a significant increase in differentiation compared with non-treated cells, but less than echistatin-only treatments (Figures 7M and 7P). Altogether, these results highlight the role of integrin receptor signaling in the regulation of hASPC adipogenesis.

We then tested if the artificial expression of *IGFBP2* in cells that natively do not express IGFBP2, such as SC hASPCs, would be sufficient to blunt their adipogenic potential. To test this, we transduced SC hASPCs with lentiviral vectors encoding for Myc-DDK-IGFBP2 or Myc-DDK, as control. Cells transduced with IGFBP2 effectively secreted IGFBP2 to the cell culture media, and this action was fully prevented by incubating the cells with a protein transport inhibitor cocktail (PTIC) containing brefeldin A and monensin^{54,55} (Figures S7M and S7N). Accordingly, a large accumulation of IGFBP2 was observed in total lysates when Myc-DDK-IGFBP2 transduced cells were treated with the PTIC (Figure S7N). These results demonstrate that our transduced SC hASPCs effectively expressed and secreted IGFBP2. When induced to differentiate, control cells showed a clear accumulation of LDs. By contrast, cells expressing IGFBP2 remained largely fusiform and only showed several small LDs (Figure S7O). Collectively, these observations indicate that the forced expression of IGFBP2 blunts adipogenic differentiation in SC hASPCs.

DISCUSSION

Here, we resolved the Lin[−] fraction of human SC, PR, OM, and MC AT by scRNA-seq. By contrasting our data with publicly available datasets from both human and mouse ATs,^{5,9} we could identify stromal populations that are shared across ATs, including three relatively small ones (*HHIP*⁺, *IFIT*⁺, and *SFRP4*⁺ cells), as well as two main ones: (1) the hASCs, which mapped to mouse and human *DPP4*⁺ populations,^{4,7,11} and (2) the hPreAs, which mapped to the mouse *Icam1*⁺/*Aoc3*⁺^{4,7} and human *ICAM1*⁺ population.⁴ Finally, a significant VSMP cluster was also found in all analyzed human adipose depots.

We also identified depot-specific populations such as the mesothelial cells, which are almost exclusive to OM AT. Although the presence of mesothelial cells within the OM SVF has been reported previously,^{5,8,10,11} their role within the ASC niche remained elusive. As previously observed in mice,³¹ our results suggest that mesothelial cells do not give rise to adipocytes. Yet, a specific subset of mesothelial cells can inhibit the differentiation of neighboring hASPCs, suggesting that the mesothelium, either surrounding or interspersed in the OM AT, could have a regulatory impact on its plasticity. This specific subpopulation, sorted as Lin[−]/TM4SF1+/MSLN^{low} cells, expressed and secreted high levels of IGFBP2 and strongly repressed the adipogenic capacity of both SC and OM hASPCs. This is consistent with IGFBP2's previously reported anti-adipogenic properties.^{32,56} Mechanistically, our findings suggest that the anti-adipogenic action of IGFBP2 is mediated by the activation of integrin receptor signaling. The ability of IGFBP2 to activate integrin receptors, especially $\alpha 5\beta 1$ heterodimers, has been well

characterized.^{57,58} Consistent with our results, the activation of these receptors by other molecules, such as fibronectin, or via overexpression of *Itga5* (encoding integrin $\alpha 5$) suppresses terminal differentiation in murine adipogenic cell lines.^{48,59,60} Accordingly, our transcriptomic analyses revealed that cultured OM SVF cells can engage the early steps of the adipogenic program but fail to effectively reach late stages. The identification of an anti-adipogenic population within the OM SVF might help explain the limited adipogenic capacity of OM SVFs in culture.^{14,61–66} However, the knockdown of *IGFBP2* only partially rescued the ability of OM hASPCs to be adipogenic, indicating that OM hASPCs still feature other cell-intrinsic mechanisms that render them refractory to differentiation *ex vivo*. In this sense, OM cells featured a more inflammatory gene expression profile, which might also explain the lower differentiation capacity of these cells. Furthermore, previous work has shown that OM-derived ASPCs secrete a larger number of TGF- β ligands and that inhibition of TGF- β signaling improves the adipogenic differentiation of OM-derived cells.⁶⁷ Notably, TGF- β can increase *IGFBP2* expression,⁶⁸ which suggests that IGFBP2 secretion could also participate in the inhibitory action of TGF- β on *de novo* adipogenesis.

Our identification of an OM-specific anti-adipogenic cell type evokes the discovery of Aregs in mouse SC AT.^{7,8,12,13} Thus, also in humans, specialized niche cells could contribute to AT plasticity. However, Aregs and OM-derived *IGFBP2+* cells have different cellular identities. Although Aregs are of mesenchymal nature, *IGFBP2+* cells expressed a joint mesenchymal and mesothelial identity and showed enrichment of mesothelial to mesenchymal transition markers, a process that can be driven by IGFBP2 itself.^{69–71} This suggests that, although cell types with homologous anti-adipogenic actions might exist in different adipose depots, they might have different transcriptional/cellular identities.

Several factors need to be considered when speculating on the potential physiological roles of *IGFBP2+* cells *in vivo*. First, these cells are a relatively small subset (~2%) of the total SVF cells within the OM AT. Therefore, their effects might be rather local. A second aspect is timing. We have recently described how Aregs acquire their anti-adipogenic capacity after weaning.¹² Consequently, we cannot rule out that the number of *IGFBP2+* cells or their anti-adipogenic properties might be modulated at different life stages, allowing to flexibly alter OM AT growth responses. Finally, additional studies will be necessary to understand the role of this new anti-adipogenic cell type in pathophysiological situations. In this sense, we observed a highly significant positive correlation between inferred *IGFBP2+* cell abundance and BMI. The latter observation appears to contrast with previous results reporting an anti-correlation between BMI,^{72–74} onset of metabolic syndrome⁷⁵ and non-alcoholic fatty liver disease⁷⁶ on the one hand and circulating IGFBP2 serum levels on the other. One possible explanation is that a higher number of *IGFBP2+* cells does not mean a higher level of expression or secretion. Also, since IGFBP2 is secreted by other organs, such as the liver,^{76,77} systemic IGFBP2 levels might not reflect IGFBP2's paracrine secretion from the OM AT.

Different proportions of hASPC subtypes might also influence hyperplastic versus hypertrophic responses in ATs. For example, we found the hASC pool to be proportionally the smallest in OM AT, supporting the hypothesis that SC and PR ATs have a greater capacity to expand through hyperplasia compared with OM

AT.^{78,79} However, the growth of different adipose depots in response to nutrients or biological cues is subjected to large inter-individual variation for any given adipose depot in terms of adipocyte size.^{80,81} Hence, although adipocyte hypertrophy, especially in OM AT, seems linked to metabolic complications, whether this particular depot grows through hypertrophy or hyperplasia might have a strong individual/genetic component. It is tempting to speculate that a different abundance of IGFBP2-expressing cells could influence whether OM AT in humans grows predominantly through hypertrophic or hyperplastic means.^{82–84}

Altogether, our work contributes to a better understanding of the behaviors of different human adipose depots. It also highlights the main cellular populations that are conserved across depots and species. And, finally, it identifies and mechanistically characterizes an OM-specific population that inhibits the differentiation of neighboring hASPCs. A recent study by Zhang et al.⁸ of mouse epididymal AT did identify “mesothelial-like cells” that shared markers with both mesothelial and mesenchymal cells and that were also defined by high *Igfbp2* expression. This suggests that OM *IGFBP2+* cells may be conserved between mouse and human, which in turn could open new experimental avenues to study their relevance in OM AT plasticity. A better understanding of the action of OM *IGFBP2+* cells could also lead to new strategies to render OM hASPCs more adipogenic and less inflammatory, which could be valuable to treat metabolic disorders linked to obesity.

Limitations of the study

Some of our mechanistic and functional assays involve the prior plating of full SVFs or sorted cellular subpopulations. We cannot rule out that our sorting strategy, as well as the plating and expansion of our cells *ex vivo*, could have influenced the transcriptomic and/or functional properties of the cells compared with their behavior in their original tissue niche. This is a common problem in scientific areas exploring primary cultures or plating cells after tissue disaggregation. In this sense, recent advances in spatial, single-cell transcriptomics^{85,86} and proteomics⁸⁷ are expected to illustrate the divergences between primary cultured cells and cells in their native environment. Another limitation is the lack of longitudinality in our biopsy sampling, preventing us from unequivocally predicting how different cellular subpopulation proportions influence the long-term composition and function of their adipose depots. It is thereby important to recognize that our study was not designed to interrogate how a particular life stage, weight, or disease influences the abundance or function of the diverse cellular subpopulations in adipose depots. Although we identified some correlations, future studies on larger, well-defined cohorts will be necessary to clearly determine the relationship between age and obesity and the proportion/function of the different cellular subpopulations, such as TM4SF1+/MLSN^{low} (*IGFBP2+*) cells.

STAR★METHODS

Detailed methods are provided in the online version of this paper and include the following:

- KEY RESOURCES TABLE
- RESOURCE AVAILABILITY
 - Lead contact

- Materials availability
- Data and code availability
- EXPERIMENTAL MODEL AND STUDY PARTICIPANT DETAILS
 - Bioethics
 - Human ASPCs isolation and culture
- METHOD DETAILS
 - Bulk RNA barcoding and sequencing (BRB-seq)
 - Analysis of BRB-seq data
 - scRNA-seq of SVF Lin⁻ cells
 - Analysis of scRNA-seq data
 - FACS sorting of human SVF subpopulations
 - *In vitro* adipogenic differentiation, chemical treatments and lentiviral infection of hASPCs
 - Cell proliferation assay
 - Mixing and transwell experiments
 - Enzyme-linked immunosorbent assay (ELISA)
 - Immunohistochemistry
 - RNAscope
 - Protein analyses
 - Imaging and quantification of *in vitro* adipogenesis
 - siRNA-mediated knockdown
 - RNA isolation and qPCR
- QUANTIFICATION AND STATISTICAL ANALYSIS

SUPPLEMENTAL INFORMATION

Supplemental information can be found online at <https://doi.org/10.1016/j.cmet.2024.04.017>.

ACKNOWLEDGMENTS

The authors thank the EPFL Core Facilities: flow cytometry (especially Miguel Garcia), bioimaging (especially Olivier Buri, Romain Guiet, and José Artacho), gene expression (especially Bastien Mangeat and Elisa Cora), and histology (especially Jessica Dessimoz). We are also grateful to the UNIL flow cytometry facility, especially Danny Labes. Open access funding provided by EPFL, a Leenaards Foundation MD-PhD Fellowship to R.F. (#531466), and a Leenaards Prize for Biomedical Translational Research to B.D. (Project #5154.5); a Personalized Health and Related Technologies (PHRT) PhD student fellowship (#2017/307) to P.Y.R.; and PHRT grants (#2017/502 and #2019/719) to B.D., as well as a Swiss National Science Foundation Project grant (#310030_182655) to B.D.

AUTHOR CONTRIBUTIONS

R.F., P.Y.R., C.C., and B.D. designed the study and wrote the manuscript. R.F., M.R., and C.C. conducted experimental procedures. P.Y.R. conducted all transcriptomic analyses. J.R. and M.Z. assisted with sample processing, cell culture, and the preparation of sequencing libraries. J.R. performed histological assays. J.P. provided assistance with flow cytometry procedures. D.A. and V.G. assisted with bulk transcriptomic procedures and analyses. V.G. and W.S. assisted with the transcriptomic analyses. L.F., S.M., T.Z., N.P., M.S., and M.M. provided access to human samples. V.G. and W.S. helped edit the manuscript.

DECLARATION OF INTERESTS

The authors declare no competing interests.

Received: May 12, 2023

Revised: December 22, 2023

Accepted: April 19, 2024

Published: May 9, 2024

REFERENCES

1. Schleinitz, D., Krause, K., Wohland, T., Gebhardt, C., Linder, N., Stumvoll, M., Blüher, M., Bechmann, I., Kovacs, P., Gericke, M., et al. (2020). Identification of distinct transcriptome signatures of human adipose tissue from fifteen depots. *Eur. J. Hum. Genet.* 28, 1714–1725. <https://doi.org/10.1038/s41431-020-0681-1>.
2. Pellegrinelli, V., Carobbio, S., and Vidal-Puig, A. (2016). Adipose tissue plasticity: how fat depots respond differently to pathophysiological cues. *Diabetologia* 59, 1075–1088. <https://doi.org/10.1007/s00125-016-3933-4>.
3. Tchkonina, T., Thomou, T., Zhu, Y., Karagiannides, I., Pothoulakis, C., Jensen, M.D., and Kirkland, J.L. (2013). Mechanisms and metabolic implications of regional differences among fat depots. *Cell Metab.* 17, 644–656. <https://doi.org/10.1016/j.cmet.2013.03.008>.
4. Merrick, D., Sakers, A., Irgebay, Z., Okada, C., Calvert, C., Morley, M.P., Percec, I., and Seale, P. (2019). Identification of a mesenchymal progenitor cell hierarchy in adipose tissue. *Science* 364, eaav2501. <https://doi.org/10.1126/science.aav2501>.
5. Emont, M.P., Jacobs, C., Essene, A.L., Pant, D., Tenen, D., Colleluori, G., Di Vincenzo, A., Jørgensen, A.M., Dashti, H., Stefek, A., et al. (2022). A single-cell atlas of human and mouse white adipose tissue. *Nature* 603, 926–933. <https://doi.org/10.1038/s41586-022-04518-2>.
6. Vijay, J., Gauthier, M.-F., Biswell, R.L., Louiselle, D.A., Johnston, J.J., Cheung, W.A., Belden, B., Pramatarova, A., Biertho, L., Gibson, M., et al. (2020). Single-cell analysis of human adipose tissue identifies depot and disease specific cell types. *Nat. Metab.* 2, 97–109. <https://doi.org/10.1038/s42255-019-0152-6>.
7. Schwalie, P.C., Dong, H., Zachara, M., Russeil, J., Alpern, D., Akchiche, N., Caprara, C., Sun, W., Schlaudraff, K.-U., Soldati, G., et al. (2018). A stromal cell population that inhibits adipogenesis in mammalian fat depots. *Nature* 559, 103–108. <https://doi.org/10.1038/s41586-018-0226-8>.
8. Zhang, Q., Shan, B., Guo, L., Shao, M., Vishvanath, L., Elmquist, G., Xu, L., and Gupta, R.K. (2022). Distinct functional properties of murine perinatal and adult adipose progenitor subpopulations. *Nat. Metab.* 4, 1055–1070. <https://doi.org/10.1038/s42255-022-00613-w>.
9. Ferrero, R., Rainer, P., and Deplancke, B. (2020). Toward a Consensus View of Mammalian Adipocyte Stem and Progenitor Cell Heterogeneity. *Trends Cell Biol.* 30, 937–950. <https://doi.org/10.1016/j.tcb.2020.09.007>.
10. Jackson-Jones, L.H., Smith, P., Portman, J.R., Magalhaes, M.S., Mylonas, K.J., Vermeren, M.M., Nixon, M., Henderson, B.E.P., Dobie, R., Vermeren, S., et al. (2020). Stromal Cells Covering Omental Fat-Associated Lymphoid Clusters Trigger Formation of Neutrophil Aggregates to Capture Peritoneal Contaminants. *Immunity* 52, 700–715.e6. <https://doi.org/10.1016/j.immuni.2020.03.011>.
11. Burl, R.B., Ramseyer, V.D., Rondini, E.A., Pique-Regi, R., Lee, Y.-H., and Granneman, J.G. (2018). Deconstructing Adipogenesis Induced by β 3-Adrenergic Receptor Activation with Single-Cell Expression Profiling. *Cell Metab.* 28, 300–309.e4. <https://doi.org/10.1016/j.cmet.2018.05.025>.
12. Zachara, M., Rainer, P.Y., Hashimi, H., Russeil, J.M., Alpern, D., Ferrero, R., Litovchenko, M., and Deplancke, B. (2022). Mammalian adipogenesis regulator (Areg) cells use retinoic acid signalling to be non- and anti-adipogenic in age-dependent manner. *EMBO J.* 41, e108206. <https://doi.org/10.15252/embj.2021108206>.
13. Dong, H., Sun, W., Shen, Y., Baláz, M., Balázová, L., Ding, L., Löffler, M., Hamilton, B., Klötting, N., Blüher, M., et al. (2022). Identification of a regulatory pathway inhibiting adipogenesis via RSPO2. *Nat. Metab.* 4, 90–105. <https://doi.org/10.1038/s42255-021-00509-1>.
14. Tchkonina, T., Giorgadze, N., Pirtskhalava, T., Tchoukalova, Y., Karagiannides, I., Forse, R.A., DePonte, M., Stevenson, M., Guo, W., Han, J., et al. (2002). Fat depot origin affects adipogenesis in primary cultured and cloned human preadipocytes. *Am. J. Physiol. Regul. Integr. Comp. Physiol.* 282, R1286–R1296. <https://doi.org/10.1152/ajpregu.00653.2001>.
15. Alpern, D., Gardeux, V., Russeil, J., Mangeat, B., Meireles-Filho, A.C.A., Breyse, R., Hacker, D., and Deplancke, B. (2019). BRB-seq: ultra-affordable high-throughput transcriptomics enabled by bulk RNA

- barcoding and sequencing. *Genome Biol.* 20, 71. <https://doi.org/10.1186/s13059-019-1671-x>.
16. Saalbach, A., and Andersregg, U. (2019). Thy-1: more than a marker for mesenchymal stromal cells. *FASEB J.* 33, 6689–6696. <https://doi.org/10.1096/fj.201802224R>.
 17. Takeda, K., Sriram, S., Chan, X.H.D., Ong, W.K., Yeo, C.R., Tan, B., Lee, S.-A., Kong, K.V., Hoon, S., Jiang, H., et al. (2016). Retinoic Acid Mediates Visceral-Specific Adipogenic Defects of Human Adipose-Derived Stem Cells. *Diabetes* 65, 1164–1178. <https://doi.org/10.2337/db15-1315>.
 18. Passaro, A., Miselli, M.A., Sanz, J.M., Dalla Nora, E., Morieri, M.L., Colonna, R., Pišot, R., and Zuliani, G. (2017). Gene expression regional differences in human subcutaneous adipose tissue. *BMC Genomics* 18, 202. <https://doi.org/10.1186/s12864-017-3564-2>.
 19. Wellen, K.E., and Hotamisligil, G.S. (2005). Inflammation, stress, and diabetes. *J. Clin. Invest.* 115, 1111–1119. <https://doi.org/10.1172/JCI25102>.
 20. Trayhurn, P., and Wood, I.S. (2004). Adipokines: inflammation and the pleiotropic role of white adipose tissue. *Br. J. Nutr.* 92, 347–355. <https://doi.org/10.1079/bjn20041213>.
 21. Arner, P. (2007). Introduction: the inflammation orchestra in adipose tissue. *J. Intern. Med.* 262, 404–407. <https://doi.org/10.1111/j.1365-2796.2007.01850.x>.
 22. Kiselev, V.Y., Yiu, A., and Hemberg, M. (2018). scmap: projection of single-cell RNA-seq data across data sets. *Nat. Methods* 15, 359–362. <https://doi.org/10.1038/nmeth.4644>.
 23. Majesky, M.W., Dong, X.R., Regan, J.N., and Hoglund, V.J. (2011). Vascular Smooth Muscle Progenitor Cells: Building and Repairing Blood Vessels. *Circ. Res.* 108, 365–377. <https://doi.org/10.1161/CIRCRESAHA.110.223800>.
 24. Yu, W., Chen, Z., Zhang, J., Zhang, L., Ke, H., Huang, L., Peng, Y., Zhang, X., Li, S., Lahn, B.T., et al. (2008). Critical role of phosphoinositide 3-kinase cascade in adipogenesis of human mesenchymal stem cells. *Mol. Cell. Biochem.* 310, 11–18. <https://doi.org/10.1007/s11010-007-9661-9>.
 25. Desarzens, S., Liao, W.-H., Mammi, C., Caprio, M., and Faresse, N. (2014). Hsp90 blockers inhibit adipocyte differentiation and fat mass accumulation. *PLoS One* 9, e94127. <https://doi.org/10.1371/journal.pone.0094127>.
 26. Peng, J., Li, Y., Wang, X., Deng, S., Holland, J., Yates, E., Chen, J., Gu, H., Essandoh, K., Mu, X., et al. (2018). An Hsp20-FBXO4 Axis Regulates Adipocyte Function through Modulating PPAR γ Ubiquitination. *Cell Rep.* 23, 3607–3620. <https://doi.org/10.1016/j.celrep.2018.05.065>.
 27. Li, R.Y., Song, H.D., Shi, W.J., Hu, S.M., Yang, Y.S., Tang, J.F., Chen, M.D., and Chen, J.L. (2004). Galanin inhibits leptin expression and secretion in rat adipose tissue and 3T3-L1 adipocytes. *J. Mol. Endocrinol.* 33, 11–19. <https://doi.org/10.1677/jme.0.0330011>.
 28. Gu, D., Yu, B., Zhao, C., Ye, W., Lv, Q., Hua, Z., Ma, J., and Zhang, Y. (2007). The effect of pleiotrophin signaling on adipogenesis. *FEBS Lett.* 581, 382–388. <https://doi.org/10.1016/j.febslet.2006.12.043>.
 29. De Silva, H.C., Firth, S.M., Twigg, S.M., and Baxter, R.C. (2012). Interaction Between IGF Binding Protein-3 and TGF β in the Regulation of Adipocyte Differentiation. *Endocrinology* 153, 4799–4807. <https://doi.org/10.1210/en.2011-1444>.
 30. Ong, W.K., Tan, C.S., Chan, K.L., Goesantoso, G.G., Chan, X.H.D., Chan, E., Yin, J., Yeo, C.R., Khoo, C.M., So, J.B.Y., et al. (2014). Identification of specific cell-surface markers of adipose-derived stem cells from subcutaneous and visceral fat depots. *Stem Cell Rep.* 2, 171–179. <https://doi.org/10.1016/j.stemcr.2014.01.002>.
 31. Westcott, G.P., Emont, M.P., Li, J., Jacobs, C., Tsai, L., and Rosen, E.D. (2021). Mesothelial cells are not a source of adipocytes in mice. *Cell Rep.* 36, 109388. <https://doi.org/10.1016/j.celrep.2021.109388>.
 32. Yau, S.W., Russo, V.C., Clarke, I.J., Dunshea, F.R., Werther, G.A., and Sabin, M.A. (2015). IGFBP-2 inhibits adipogenesis and lipogenesis in human visceral, but not subcutaneous, adipocytes. *Int. J. Obes. (Lond)* 39, 770–781. <https://doi.org/10.1038/ijo.2014.192>.
 33. Xi, G., Solum, M.A., Wai, C., Maile, L.A., Rosen, C.J., and Clemmons, D.R. (2013). The Heparin-Binding Domains of IGFBP-2 Mediate Its Inhibitory Effect on Preadipocyte Differentiation and Fat Development in Male Mice. *Endocrinology* 154, 4146–4157. <https://doi.org/10.1210/en.2013-1236>.
 34. Wang, F., Flanagan, J., Su, N., Wang, L.-C., Bui, S., Nielson, A., Wu, X., Vo, H.-T., Ma, X.-J., and Luo, Y. (2012). RNAscope: a novel in situ RNA analysis platform for formalin-fixed, paraffin-embedded tissues. *J. Mol. Diagn.* 14, 22–29. <https://doi.org/10.1016/j.jmoldx.2011.08.002>.
 35. Wolf, F.A., Hamey, F.K., Plass, M., Solana, J., Dahlin, J.S., Göttgens, B., Rajewsky, N., Simon, L., and Theis, F.J. (2019). PAGA: graph abstraction reconciles clustering with trajectory inference through a topology preserving map of single cells. *Genome Biol.* 20, 59. <https://doi.org/10.1186/s13059-019-1663-x>.
 36. Yang, J., Antin, P., Bex, G., Blanpain, C., Brabletz, T., Bronner, M., Campbell, K., Cano, A., Casanova, J., Christofori, G., et al. (2020). Guidelines and definitions for research on epithelial–mesenchymal transition. *Nat. Rev. Mol. Cell Biol.* 21, 341–352. <https://doi.org/10.1038/s41580-020-0237-9>.
 37. Nisticò, P., Bissell, M.J., and Radisky, D.C. (2012). Epithelial-Mesenchymal Transition: General Principles and Pathological Relevance with Special Emphasis on the Role of Matrix Metalloproteinases. *Cold Spring Harb. Perspect. Biol.* 4, a011908. <https://doi.org/10.1101/cshperspect.a011908>.
 38. Weber, C.E., Li, N.Y., Wai, P.Y., and Kuo, P.C. (2012). Epithelial-Mesenchymal Transition, TGF- β , and Osteopontin in Wound Healing and Tissue Remodeling After Injury. *J. Burn Care Res.* 33, 311–318. <https://doi.org/10.1097/BCR.0b013e318240541e>.
 39. Marconi, G.D., Fonticoli, L., Rajan, T.S., Pierdomenico, S.D., Trubiani, O., Pizzicannella, J., and Diomedea, F. (2021). Epithelial-Mesenchymal Transition (EMT): The Type-2 EMT in Wound Healing, Tissue Regeneration and Organ Fibrosis. *Cells* 10, 1587. <https://doi.org/10.3390/cells10071587>.
 40. Tsai, J.M., Sinha, R., Seita, J., Fernhoff, N., Christ, S., Koopmans, T., Krampitz, G.W., McKenna, K.M., Xing, L., Sandholzer, M., et al. (2018). Surgical adhesions in mice are derived from mesothelial cells and can be targeted by antibodies against mesothelial markers. *Sci. Transl. Med.* 10, eaan6735. <https://doi.org/10.1126/scitranslmed.aan6735>.
 41. Yang, R.-Z., Lee, M.-J., Hu, H., Pray, J., Wu, H.-B., Hansen, B.C., Shuldiner, A.R., Fried, S.K., McLenithan, J.C., and Gong, D.-W. (2006). Identification of omentin as a novel depot-specific adipokine in human adipose tissue: possible role in modulating insulin action. *Am. J. Physiol. Endocrinol. Metab.* 290, E1253–E1261. <https://doi.org/10.1152/ajpendo.00572.2004>.
 42. Schäffler, A., Neumeier, M., Herfarth, H., Fürst, A., Schölmerich, J., and Büchler, C. (2005). Genomic structure of human omentin, a new adipocyte-tokine expressed in omental adipose tissue. *Biochim. Biophys. Acta* 1732, 96–102. <https://doi.org/10.1016/j.bbaexp.2005.11.005>.
 43. Boughanem, H., Yubero-Serrano, E.M., López-Miranda, J., Tinahones, F.J., and Macias-Gonzalez, M. (2021). Potential Role of Insulin Growth-Factor-Binding Protein 2 as Therapeutic Target for Obesity-Related Insulin Resistance. *Int. J. Mol. Sci.* 22, 1133. <https://doi.org/10.3390/ijms22031133>.
 44. Hesse, D., Trost, J., Schäfer, N., Schwerbel, K., Hoefflich, A., Schürmann, A., and Brockmann, G.A. (2018). Effect of adipocyte-derived IGF-I on adipose tissue mass and glucose metabolism in the Berlin Fat Mouse. *Growth Factors* 36, 78–88. <https://doi.org/10.1080/08977194.2018.1497621>.
 45. Wang, F., Li, H., Lou, Y., Xie, J., Cao, D., and Huang, X. (2019). Insulin-like growth factor I promotes adipogenesis in hemangioma stem cells from infantile hemangiomas. *Mol. Med. Rep.* 19, 2825–2830. <https://doi.org/10.3892/mmr.2019.9895>.

46. Zhang, K., Wang, F., Huang, J., Lou, Y., Xie, J., Li, H., Cao, D., and Huang, X. (2019). Insulin-like growth factor 2 promotes the adipogenesis of hemangioma-derived stem cells. *Exp. Ther. Med.* 17, 1663–1669. <https://doi.org/10.3892/etm.2018.7132>.
47. Alfares, M.N., Perks, C.M., Hamilton-Shield, J.P., and Holly, J.M.P. (2018). Insulin-like growth factor-II in adipocyte regulation: depot-specific actions suggest a potential role limiting excess visceral adiposity. *Am. J. Physiol. Endocrinol. Metab.* 315, E1098–E1107. <https://doi.org/10.1152/ajpendo.00409.2017>.
48. Uetaki, M., Onishi, N., Oki, Y., Shimizu, T., Sugihara, E., Sampetean, O., Watanabe, T., Yanagi, H., Suda, K., Fujii, H., et al. (2022). Regulatory roles of fibronectin and integrin $\alpha 5$ in reorganization of the actin cytoskeleton and completion of adipogenesis. *Mol. Biol. Cell* 33, ar78. <https://doi.org/10.1091/mbc.E21-12-0609>.
49. Kumar, C.C., Nie, H., Rogers, C.P., Malkowski, M., Maxwell, E., Catino, J.J., and Armstrong, L. (1997). Biochemical characterization of the binding of echistatin to integrin $\alpha v \beta 3$ receptor. *J. Pharmacol. Exp. Ther.* 283, 843–853.
50. Wei, Y., Tang, C.-H., Kim, Y., Robillard, L., Zhang, F., Kugler, M.C., and Chapman, H.A. (2007). Urokinase receptors are required for $\alpha 5 \beta 1$ integrin-mediated signaling in tumor cells. *J. Biol. Chem.* 282, 3929–3939. <https://doi.org/10.1074/jbc.M607989200>.
51. Luo, S., Shi, Q., Li, W., Wu, W., and Zha, Z. (2020). ITGB1 promotes the chondrogenic differentiation of human adipose-derived mesenchymal stem cells by activating the ERK signaling. *J. Mol. Histol.* 51, 729–739. <https://doi.org/10.1007/s10735-020-09918-0>.
52. Tseng, C., and Kolonin, M.G. (2016). Proteolytic Isoforms of SPARC Induce Adipose Stromal Cell Mobilization in Obesity. *Stem Cells Dayt. Ohio* 34, 174–190. <https://doi.org/10.1002/stem.2192>.
53. Farnier, C., Krief, S., Blache, M., Diot-Dupuy, F., Mory, G., Ferre, P., and Bazin, R. (2003). Adipocyte functions are modulated by cell size change: potential involvement of an integrin/ERK signalling pathway. *Int. J. Obes. Relat. Metab. Disord.* 27, 1178–1186. <https://doi.org/10.1038/sj.ijo.0802399>.
54. Helms, J.B., and Rothman, J.E. (1992). Inhibition by brefeldin A of a Golgi membrane enzyme that catalyses exchange of guanine nucleotide bound to ARF. *Nature* 360, 352–354. <https://doi.org/10.1038/360352a0>.
55. Pohlmann, R., Krüger, S., Hasilik, A., and Von Figura, K. (1984). Effect of monensin on intracellular transport and receptor-mediated endocytosis of lysosomal enzymes. *Biochem. J.* 217, 649–658. <https://doi.org/10.1042/bj2170649>.
56. Russo, V.C., Azar, W.J., Yau, S.W., Sabin, M.A., and Werther, G.A. (2015). IGFBP-2: The dark horse in metabolism and cancer. *Cytokine Growth Factor Rev.* 26, 329–346. <https://doi.org/10.1016/j.cytogfr.2014.12.001>.
57. Wang, G.K., Hu, L., Fuller, G.N., and Zhang, W. (2006). An interaction between insulin-like growth factor-binding protein 2 (IGFBP2) and integrin $\alpha 5$ is essential for IGFBP2-induced cell mobility. *J. Biol. Chem.* 281, 14085–14091. <https://doi.org/10.1074/jbc.M513686200>.
58. Schütt, B.S., Langkamp, M., Rauschnabel, U., Ranke, M.B., and Elminger, M.W. (2004). Integrin-mediated action of insulin-like growth factor binding protein-2 in tumor cells. *J. Mol. Endocrinol.* 32, 859–868. <https://doi.org/10.1677/jme.0.0320859>.
59. Liu, J., DeYoung, S.M., Zhang, M., Zhang, M., Cheng, A., and Saltiel, A.R. (2005). Changes in integrin expression during adipocyte differentiation. *Cell Metab.* 2, 165–177. <https://doi.org/10.1016/j.cmet.2005.08.006>.
60. Wang, Y., Zhao, L., Smas, C., and Sul, H.S. (2010). Pref-1 interacts with fibronectin to inhibit adipocyte differentiation. *Mol. Cell. Biol.* 30, 3480–3492. <https://doi.org/10.1128/MCB.00057-10>.
61. Hauner, H., Wabitsch, M., and Pfeiffer, E.F. (1988). Differentiation of adipocyte precursor cells from obese and nonobese adult women and from different adipose tissue sites. *Horm. Metab. Res. Suppl.* 19, 35–39.
62. Tchkonina, T., Giorgadze, N., Pirtskhalava, T., Thomou, T., DePonte, M., Koo, A., Forse, R.A., Chinnappan, D., Martin-Ruiz, C., von Zglinicki, T., et al. (2006). Fat depot-specific characteristics are retained in strains derived from single human preadipocytes. *Diabetes* 55, 2571–2578. <https://doi.org/10.2337/db06-0540>.
63. Digby, J.E., Crowley, V.E., Sewter, C.P., Whitehead, J.P., Prins, J.B., and O’rahilly, S. (2000). Depot-related and thiazolidinedione-responsive expression of uncoupling protein 2 (UCP2) in human adipocytes. *Int. J. Obes. Relat. Metab. Disord.* 24, 585–592. <https://doi.org/10.1038/sj.ijo.0801201>.
64. Belligoli, A., Compagnin, C., Sanna, M., Favaretto, F., Fabris, R., Busetto, L., Foletto, M., Dal Prà, C., Serra, R., Prevedello, L., et al. (2019). Characterization of subcutaneous and omental adipose tissue in patients with obesity and with different degrees of glucose impairment. *Sci. Rep.* 9, 11333. <https://doi.org/10.1038/s41598-019-47719-y>.
65. Baglioni, S., Cantini, G., Poli, G., Francelanci, M., Squecco, R., Di Franco, A., Borgogni, E., Frontera, S., Nesi, G., Liotta, F., et al. (2012). Functional Differences in Visceral and Subcutaneous Fat Pads Originate from Differences in the Adipose Stem Cell. *PLoS One* 7, e36569. <https://doi.org/10.1371/journal.pone.0036569>.
66. Baer, P.C. (2014). Adipose-derived mesenchymal stromal/stem cells: Anan update on their phenotype in vivo and in vitro. *World J. Stem Cells* 6, 256–265. <https://doi.org/10.4252/wjsc.v6.i3.256>.
67. Lee, M.-J., Pickering, R.T., Shibad, V., Wu, Y., Karastergiou, K., Jager, M., Layne, M.D., and Fried, S.K. (2019). Impaired Glucocorticoid Suppression of TGF β Signaling in Human Omental Adipose Tissues Limits Adipogenesis and May Promote Fibrosis. *Diabetes* 68, 587–597. <https://doi.org/10.2337/db18-0955>.
68. Guo, Y.S., Townsend, C.M., Jin, G.F., Beauchamp, R.D., and Thompson, J.C. (1995). Differential regulation by TGF- β 1 and insulin of insulin-like growth factor binding protein-2 in IEC-6 cells. *Am. J. Physiol.* 268, E1199–E1204. <https://doi.org/10.1152/ajpendo.1995.268.6.E1199>.
69. Koopmans, T., and Rinkevich, Y. (2018). Mesothelial to mesenchyme transition as a major developmental and pathological player in trunk organs and their cavities. *Commun. Biol.* 1, 170. <https://doi.org/10.1038/s42003-018-0180-x>.
70. Zhu, H., Zhang, Y., Geng, Y., Lu, W., Yin, J., Li, Z., Huang, L., Liu, H., and Xu, N. (2019). IGFBP2 promotes the EMT of colorectal cancer cells by regulating E-cadherin expression. *Int. J. Clin. Exp. Pathol.* 12, 2559–2565.
71. Haschemi, R., Kobelt, D., Steinwarz, E., Schlesinger, M., Stein, U., and Bendas, G. (2021). Insulin-like Growth Factor Binding Protein-2 (IGFBP2) Is a Key Molecule in the MACC1-Mediated Platelet Communication and Metastasis of Colorectal Cancer Cells. *Int. J. Mol. Sci.* 22, 12195. <https://doi.org/10.3390/ijms222212195>.
72. van den Beld, A.W., Carlson, O.D., Doyle, M.E., Rizopoulos, D., Ferrucci, L., van der Lely, A.J., and Egan, J.M. (2019). IGFBP-2 and aging: a 20-year longitudinal study on IGFBP-2, IGF-I, BMI, insulin sensitivity and mortality in an aging population. *Eur. J. Endocrinol.* 180, 109–116. <https://doi.org/10.1530/EJE-18-0422>.
73. Wheatcroft, S.B., Kearney, M.T., Shah, A.M., Ezzat, V.A., Miell, J.R., Modo, M., Williams, S.C.R., Cawthorn, W.P., Medina-Gomez, G., Vidal-Puig, A., et al. (2007). IGF-Binding Protein-2 Protects Against the Development of Obesity and Insulin Resistance. *Diabetes* 56, 285–294. <https://doi.org/10.2337/db06-0436>.
74. Hedbacker, K., Birsoy, K., Wysocki, R.W., Asilmaz, E., Ahima, R.S., Farooqi, I.S., and Friedman, J.M. (2010). Antidiabetic Effects of IGFBP2, a Leptin-Regulated Gene. *Cell Metab.* 11, 11–22. <https://doi.org/10.1016/j.cmet.2009.11.007>.
75. Heald, A.H., Kaushal, K., Siddals, K.W., Rudenski, A.S., Anderson, S.G., and Gibson, J.M. (2006). Insulin-like growth factor binding protein-2 (IGFBP-2) is a marker for the metabolic syndrome. *Exp. Clin. Endocrinol. Diabetes* 114, 371–376. <https://doi.org/10.1055/s-2006-924320>.
76. Fahlbusch, P., Knebel, B., Hörbelt, T., Barbosa, D.M., Nikolic, A., Jacob, S., Al-Hasani, H., Van de Velde, F., Van Nieuwenhove, Y., Müller-Wieland, D., et al. (2020). Physiological Disturbance in Fatty Liver Energy Metabolism Converges on IGFBP2 Abundance and Regulation

- in Mice and Men. *Int. J. Mol. Sci.* 21, 4144. <https://doi.org/10.3390/ijms21114144>.
77. Carter, S., Li, Z., Lemieux, I., Alm eras, N., Tremblay, A., Bergeron, J., Poirier, P., Deshaies, Y., Despr es, J.-P., and Picard, F. (2014). Circulating IGFBP-2 levels are incrementally linked to correlates of the metabolic syndrome and independently associated with VLDL triglycerides. *Atherosclerosis* 237, 645–651. <https://doi.org/10.1016/j.atherosclerosis.2014.09.022>.
 78. Sakers, A., De Siqueira, M.K., Seale, P., and Villanueva, C.J. (2022). Adipose-tissue plasticity in health and disease. *Cell* 185, 419–446. <https://doi.org/10.1016/j.cell.2021.12.016>.
 79. Kim, S.M., Lun, M., Wang, M., Senyo, S.E., Guillemier, C., Patwari, P., and Steinhilber, M.L. (2014). Loss of white adipose hyperplastic potential is associated with enhanced susceptibility to insulin resistance. *Cell Metab.* 20, 1049–1058. <https://doi.org/10.1016/j.cmet.2014.10.010>.
 80. Weyer, C., Foley, J.E., Bogardus, C., Tataranni, P.A., and Pratley, R.E. (2000). Enlarged subcutaneous abdominal adipocyte size, but not obesity itself, predicts type II diabetes independent of insulin resistance. *Diabetologia* 43, 1498–1506. <https://doi.org/10.1007/s001250051560>.
 81. Tchoukalova, Y.D., Koutsari, C., Karpayak, M.V., Votruba, S.B., Wendland, E., and Jensen, M.D. (2008). Subcutaneous adipocyte size and body fat distribution. *Am. J. Clin. Nutr.* 87, 56–63. <https://doi.org/10.1093/ajcn/87.1.56>.
 82. Drolet, R., Richard, C., Sniderman, A.D., Mailloux, J., Fortier, M., Huot, C., Rh eume, C., and Tchernof, A. (2008). Hypertrophy and hyperplasia of abdominal adipose tissues in women. *Int. J. Obes. (Lond)* 32, 283–291. <https://doi.org/10.1038/sj.jco.0803708>.
 83. Arner, P., Andersson, D.P., Th orne, A., Wir en, M., Hoffstedt, J., N aslund, E., Thorell, A., and Ryd en, M. (2013). Variations in the size of the major omentum are primarily determined by fat cell number. *J. Clin. Endocrinol. Metab.* 98, E897–E901. <https://doi.org/10.1210/jc.2012-4106>.
 84. Boivin, A., Brochu, G., Marceau, S., Marceau, P., Hould, F.-S., and Tchernof, A. (2007). Regional differences in adipose tissue metabolism in obese men. *Metabolism* 56, 533–540. <https://doi.org/10.1016/j.metabol.2006.11.015>.
 85. Merritt, C.R., Ong, G.T., Church, S.E., Barker, K., Danaher, P., Geiss, G., Hoang, M., Jung, J., Liang, Y., McKay-Fleisch, J., et al. (2020). Multiplex digital spatial profiling of proteins and RNA in fixed tissue. *Nat. Biotechnol.* 38, 586–599. <https://doi.org/10.1038/s41587-020-0472-9>.
 86. St ahl, P.L., Salm en, F., Vickovic, S., Lundmark, A., Navarro, J.F., Magnusson, J., Giacomello, S., Asp, M., Westholm, J.O., Huss, M., et al. (2016). Visualization and analysis of gene expression in tissue sections by spatial transcriptomics. *Science* 353, 78–82. <https://doi.org/10.1126/science.aaf2403>.
 87. Rosenberger, F.A., Thielert, M., Strauss, M.T., Schweizer, L., Ammar, C., M adler, S.C., Metousis, A., Skowronek, P., Wahle, M., Madden, K., et al. (2023). Spatial single-cell mass spectrometry defines zonation of the hepatocyte proteome. *Nat. Methods* 20, 1530–1536. <https://doi.org/10.1038/s41592-023-02007-6>.
 88. McCarthy, D.J., Chen, Y., and Smyth, G.K. (2012). Differential expression analysis of multifactor RNA-Seq experiments with respect to biological variation. *Nucleic Acids Res.* 40, 4288–4297. <https://doi.org/10.1093/nar/gks042>.
 89. Ritchie, M.E., Phipson, B., Wu, D., Hu, Y., Law, C.W., Shi, W., and Smyth, G.K. (2015). limma powers differential expression analyses for RNA-seq and microarray studies. *Nucleic Acids Res.* 43, e47. <https://doi.org/10.1093/nar/gkv007>.
 90. Love, M.I., Huber, W., and Anders, S. (2014). Moderated estimation of fold change and dispersion for RNA-seq data with DESeq2. *Genome Biol.* 15, 550. <https://doi.org/10.1186/s13059-014-0550-8>.
 91. Yu, G., Wang, L.-G., Han, Y., and He, Q.-Y. (2012). clusterProfiler: an R package for comparing biological themes among gene clusters. *OMICS* 16, 284–287. <https://doi.org/10.1089/omi.2011.0118>.
 92. Butler, A., Hoffman, P., Smibert, P., Papalexi, E., and Satija, R. (2018). Integrating single-cell transcriptomic data across different conditions, technologies, and species. *Nat. Biotechnol.* 36, 411–420. <https://doi.org/10.1038/nbt.4096>.
 93. Dewey, M. (2022). metap: meta-analysis of significance values. R package version 1.8. CRAN. <https://cran.r-project.org/web/packages/metap/index.html>.
 94. Hepler, C., Shao, M., Xia, J.Y., Ghaben, A.L., Pearson, M.J., Vishvanath, L., Sharma, A.X., Morley, T.S., Holland, W.L., and Gupta, R.K. (2017). Directing visceral white adipocyte precursors to a thermogenic adipocyte fate improves insulin sensitivity in obese mice. *eLife* 6, e27669. <https://doi.org/10.7554/eLife.27669>.
 95. McGinnis, C.S., Patterson, D.M., Winkler, J., Conrad, D.N., Hein, M.Y., Srivastava, V., Hu, J.L., Morrow, L.M., Weissman, J.S., Werb, Z., et al. (2019). MULTI-seq: sample multiplexing for single-cell RNA sequencing using lipid-tagged indices. *Nat. Methods* 16, 619–626. <https://doi.org/10.1038/s41592-019-0433-8>.
 96. Wolf, F.A., Angerer, P., and Theis, F.J. (2018). SCANPY: large-scale single-cell gene expression data analysis. *Genome Biol.* 19, 15. <https://doi.org/10.1186/s13059-017-1382-0>.
 97. Jacomy, M., Venturini, T., Heymann, S., and Bastian, M. (2014). ForceAtlas2, a Continuous Graph Layout Algorithm for Handy Network Visualization Designed for the Gephi Software. *PLoS One* 9, e98679. <https://doi.org/10.1371/journal.pone.0098679>.
 98. Saelens, W., Cannoodt, R., Todorov, H., and Saeys, Y. (2019). A comparison of single-cell trajectory inference methods. *Nat. Biotechnol.* 37, 547–554. <https://doi.org/10.1038/s41587-019-0071-9>.
 99. Collon, K., Gallo, M.C., Bell, J.A., Chang, S.W., Rodman, J.C.S., Sugiyama, O., Kohn, D.B., and Lieberman, J.R. (2022). Improving Lentiviral Transduction of Human Adipose-Derived Mesenchymal Stem Cells. *Hum. Gene Ther.* 33, 1260–1268. <https://doi.org/10.1089/hum.2022.117>.
 100. Boutant, M., Joffraud, M., Kulkarni, S.S., Garcia-Casarrubios, E., Garcia-Roves, P.M., Ratajczak, J., Fern andez-Marcos, P.J., Valverde, A.M., Serrano, M., and Cant o, C. (2015). SIRT1 enhances glucose tolerance by potentiating brown adipose tissue function. *Mol. Metab.* 4, 118–131. <https://doi.org/10.1016/j.molmet.2014.12.008>.

STAR★METHODS

KEY RESOURCES TABLE

REAGENT or RESOURCE	SOURCE	IDENTIFIER
Antibodies		
CD45 - Pacific Blue	Biolegend	Cat# 304022; RRID:AB_493655
CD31 - Pacific Blue	Biolegend	Cat# 303114; RRID:AB_2114316
CD26 - PE/Cy7	Biolegend	Cat# 302714; RRID:AB_2563993
VAP-1 - AF488	R&D	Cat# IC39571G; RRID:AB_3097725
MSLN (uncoupled)	Biolegend	Cat# 530101; RRID:AB_2571908
TM4SF1/L6 - AF647	R&D	Cat# FAB8164R; RRID:AB_3097728
TM4SF1/L6 - AF488	R&D	Cat# FAB8164G; RRID:AB_3097727
PLIN1 (uncoupled)	Abcam	Cat# ab172907; RRID:AB_3094446
HHIP (uncoupled)	Sigma Aldrich	Cat# WH0064399M1; RRID:AB_1841939
p44/42 MAPK (Erk1/2)	Cell Signaling	Cat# 9102; RRID:AB_330744
Phospho-p44/42 MAPK (Erk1/2) (Thr202/Tyr204)	Cell Signaling	Cat# 9101; RRID:AB_331646
Nucleoporin	BD	Cat# 610497; RRID:AB_397863
FLAG DDK	Origene	Cat# TA50011; RRID:AB_2622345
Anti-Rabbit IgG (H+L)	Thermo	Cat# A-31573; RRID:AB_2536183
Anti-Rabbit HRP	Jackson	Cat# 711-035-152; RRID:AB_10015282
Anti-Mouse HRP	Jackson	Cat# 715-035-150; RRID:AB_2340770
Bacterial and virus strains		
Myc-DDK lentiviral particles	Origene	PS100064V
Myc-DDK tagged IGFBP2 lentiviral particles	Origene	RC202573L1V
Chemicals, peptides, and recombinant proteins		
Liberase TM	Roche	05401119001
DPBS + Ca ²⁺ + Mg ²⁺	Gibco	14040091
DPBS	Gibco	14190094
Human Albumin Solution 20%	CSL Behring	3665734
VersaLyse solution	Beckman Coulter	A09777
MEMalpha GlutaMAX	Gibco	32561037
DMEM high glucose, GlutaMAX	Gibco	61965026
Human Platelet Lysate	Sigma	SCM152
Primocin	InvivoGen	ant-pm-2
3-Isobutyl-1-methylxanthine (IBMX)	Sigma Aldrich	15879
Dexamethasone	Sigma Aldrich	D2915
Insulin	Sigma Aldrich	19278
Indomethacin	Sigma Aldrich	I7378
TrypLE Select Reagent	Gibco	12563011
OPTI-Pro serum-free medium	Gibco	12309050
TRlzol	Sigma Aldrich	T3934
SuperScript™ II Reverse Transcriptase	Lifetech	18064014
RNAse H	NEB	M0297S
<i>E. coli</i> DNA ligase	NEB	M0205L
<i>E. coli</i> DNA polymerase	NEB	M0209L
NEB Next High-Fidelity 2x PCR Master Mix	NEB	M0541L
Cryomatrix	Thermo	6769006
Propidium iodide	Molecular Probes	P3566

(Continued on next page)

Continued

REAGENT or RESOURCE	SOURCE	IDENTIFIER
Compensation beads for single stains	eBiosciences	01-2222-42
Recombinant IGFBP2	R&D	674-B2-025
Recombinant IGF-I	Sigma Aldrich	I3769
Recombinant IGF-II	R&D	292-G2-050
Echistatin	R&D	3202
Lentiboost	Sirion Biotech	SB-A-LF-901-02
Protamine Sulfate	Sigma Aldrich	1101230005
Protein transport inhibitor cocktail	eBioscience	00-4980-93
Paraformaldehyde	EMS	15710
TritonX100	Sigma Aldrich	T9284
DAPI	Sigma Aldrich	D9564
Fluoromount G	Southern Biotech	0100-01
RIPA buffer	Sigma Aldrich	20-188
Protease inhibitors	Roche	11873580001
Phosphatase inhibitors	Roche	04906837001
Bodipy	Invitrogen	D3922
Hoechst	Sigma Aldrich	B2883
Fluorobrite DMEM	Gibco	A1896701
Opti-MEM medium	Invitrogen	31985062
Lipofectamine RNAiMAX	Invitrogen	13778150
SYBR Green Master Mix	Thermo	A25743
TSA Opal650	Akoya Biosciences	FP1496001KT
TSA Opal570	Akoya Biosciences	FP1488001KT
TSA Opal520	Akoya Biosciences	FP1487001KT

Critical commercial assays

Direct-ZOL	Zymo	R2054 and R2062
DNA Clean and Concentrator kit	Zymo	D4014
High Sensitivity NGS Fragment Analysis kit	Advanced Analytical	DNF-474
Qubit dsDNA HS Assay kit	Invitrogen	A32851
High Output v2 kit	Illumina	FC-404-2005
Anti-human IGFBP2 ELISA kit	Sigma Aldrich	RAB0233-1KT
Qubit™ Protein Broad Range assay kit	Thermo	A50669
SuperScript II VILO cDNA Synthesis kit	Invitrogen	11754050
Pierce BCA Protein Assay kit	Thermo	23227
BRB-seq Library preparation kits for Illumina®	Alithea Genomics	#10813
Chromium Next GEM Single Cell 3' Kit v3.1, 16 rxns	10X Genomics	PN-1000268

Deposited data

bulk RNA-seq datasets	https://www.ebi.ac.uk/biostudies/arrayexpress/studies/E-MTAB-12898?key=be3e491c-ebda-470b-9ecd-4fd6d8fcb726
scRNA-seq datasets	https://www.ebi.ac.uk/biostudies/arrayexpress/studies/E-MTAB-12893?key=ea3128af-65da-4cea-a389-12b993e0f7b7

Oligonucleotides

IGFBP2 Fw: CGAGGGCACTTGTGAGAAGCG Rv: TGTCATGGTGCTGTCCACGTG	Integrated DNA technologies	N/A
---	-----------------------------	-----

(Continued on next page)

Continued

REAGENT or RESOURCE	SOURCE	IDENTIFIER
<i>HPRT</i> Fw: CAGCCCTGGCGTCGTGATTA Rv: GTGATGGCCTCCCATCTCCTT	Integrated DNA technologies	N/A
TriFECTa RNAi Kit	Integrated DNA technologies	hs.Ri.IGFBP2.13
Hs 3plex positive control	Bio-technie	320861
Hs 3Plex negative control	Bio-technie	3200871
Hs IGFBP2-C1	Bio-technie	313061
Hs MSLN-C2	Bio-technie	413101-C2
Hs DPP4-C3	Bio-technie	477541-C3
Software and algorithms		
GraphPad Prism	https://www.graphpad.com/	N/A
RStudio	https://www.r-project.org/	N/A

RESOURCE AVAILABILITY

Lead contact

Further information and requests for resources and reagents should be directed to the lead contact, Prof. Bart Deplancke ([bart.deplancke@epfl.ch](mailto:deplancke@epfl.ch)).

Materials availability

This study did not generate new unique reagents

Data and code availability

- All of the data supporting this study are included in the article. All scRNA-Seq and BRB-Seq data have been deposited and are publicly available: <https://www.ebi.ac.uk/biostudies/arrayexpress/studies/E-MTAB-12898?key=be3e491c-ebda-470b-9ecd-4fd6d8fcb726> – Unprocessed data underlying the display items in the manuscript, related to **Figures 1, 3, S1, and S5**; <https://www.ebi.ac.uk/biostudies/arrayexpress/studies/E-MTAB-12893?key=ea3128af-65da-4cea-a389-12b993e0f7b7> – Unprocessed data underlying the display items in the manuscript, related to **Figures 2, 3, 4, 5, 6, S2–S4, and S6**; All Raw Data used to generate the figures throughout the manuscript can be found within the **Data S1** document
- All original code has been deposited at [repository] and is publicly available as of the date of publication (https://github.com/PernilleYR/hASPCs_atlas)
- Any additional information required to reanalyze the data reported in this paper is available from the **lead contact** upon request

EXPERIMENTAL MODEL AND STUDY PARTICIPANT DETAILS

Bioethics

All materials used in this study have been obtained from AT donors from two independent cohorts: the Cohort of Obese Patients of Lausanne with ethically approved license by the commission of the Vaud Canton (CER-VD Project PB_2018-00119) and a control healthy cohort from renal transplantation donors with ethically approved license by the commission of the Vaud Canton (CER-VD 2020-02021). The coded samples were collected undersigned informed consent conforming to the guidelines of the 2000 Helsinki declaration. **Table S3** illustrates cohorts demographics.

Human ASPCs isolation and culture

2–3 cm³ biopsies from SC, OM, PR and MC ATs were washed in PBS to remove excess blood, weighted and finely minced using scissors. Minced adipose tissue was incubated with 0.28 U/ml of Liberase TM (Roche #05401119001) in DPBS with calcium and magnesium (Gibco #14040091) for 60 min at 37 °C under agitation. Vigorous shaking was performed after 45 min of incubation to increase the yield of recovered SVF cells. The digested tissue was mixed with an equal volume of 1% human albumin (CSL Behring) in DPBS –/– (Gibco #14190094) to stop the lysis. Following a 5-min centrifugation at 400 g at room temperature, floating lipids and mature adipocytes were discarded by aspiration and the resuspended SVF pellet was sequentially filtered through 100-µm and 40-µm cell strainers to ensure a single cell preparation. To lyse red blood cells, pelleted SVF was resuspended in VersaLyse solution (Beckman Coulter #A09777) according to the manufacturer's recommendations and washed once with 1% albumin solution. Obtained red blood cell-free SVF suspension was systematically profiled by flow cytometry, and either plated for experiments, expanded and cryoprotected or coupled to the sorting of specific populations (see below). The SVF used for expansion or experiments was plated at a density of at least 100'000 cells per square centimeter in high glucose MEMalpha GlutaMax medium (Gibco

#32561037) supplemented with 5% human platelet lysate (Sigma #SCM152) and 50 $\mu\text{g}/\text{ml}$ Primocin (InvivoGen #ant-pm-2). For culturing human ASPCs, TryPLE Select reagent (Gibco #12563011) was used to collect the cells from the cell culture plates.

METHOD DETAILS

Bulk RNA barcoding and sequencing (BRB-seq)

All cells for BRB-seq were seeded in parallel in six 24-well plates. Cells from three wells were harvested undifferentiated (t0 time point) upon cell expansion in the 24-well plate. Cells from the three remaining wells were expanded until confluence and harvested in TRIzol (Sigma, #T3934) after 14 days of adipogenic differentiation (t14 time point). RNA was extracted from all samples in parallel using the Direct-ZOL 96 well plate format (Zymo, #R2054), and BRB-seq libraries were prepared as previously described¹⁵ and further detailed by the Mercurius™ Protocol (Alithea Genomics). In brief, 7–200 ng of total RNA from each sample was reverse transcribed in a 96-well plate using SuperScript™ II Reverse Transcriptase (Lifetech 18064014) with individual barcoded oligo-dT primers, featuring a 12-nt-long sample barcode (IDT). Double-stranded cDNA was generated by second-strand synthesis via the nick translation method using a mix containing 2 μl of RNase H (NEB, #M0297S), 1 μl of *E. coli* DNA ligase (NEB, #M0205 L), 5 μl of *E. coli* DNA Polymerase (NEB, #M0209 L), 1 μl of dNTP (10 mM), 10 μl of 5x Second Strand Buffer (100 mM Tris, pH 6.9, (AppliChem, #A3452); 25 mM MgCl_2 (Sigma, #M2670); 450 mM KCl (AppliChem, #A2939); 0.8 mM β -NAD (Sigma, N1511); 60 mM $(\text{NH}_4)_2\text{SO}_4$ (Fisher Scientific Acros, #AC20587); and 11 μl of water was added to 20 μl of Exol-treated first-strand reaction on ice. The reaction was incubated at 16 °C for 2.5 h. Full-length double-stranded cDNA was purified with 30 μl (0.6x) of AMPure XP magnetic beads (Beckman Coulter, #A63881) and eluted in 20 μl of water.

The Illumina-compatible libraries were prepared by tagmentation of 10–40 ng of full-length double-stranded cDNA with 1 μl of in-house produced Tn5 enzyme (11 μM). After tagmentation, the libraries were purified with DNA Clean and Concentrator kit (Zymo Research #D4014) eluted in 20 μl of water and PCR amplified using 25 μl NEB Next High-Fidelity 2x PCR Master Mix (NEB, #M0541 L), 2.5 μl of each i5 and i7 Illumina index adapter (IDT) using the following program: incubation 72 °C—3 min, denaturation 98 °C—30 s; 15 cycles: 98 °C—10 s, 63 °C—30 s, 72 °C—30 s; final elongation at 72 °C—5 min. The libraries were purified twice with AMPure beads (Beckman Coulter, #A63881) at a 0.6x ratio to remove the fragments < 300 nt. The resulting libraries were profiled using a High Sensitivity NGS Fragment Analysis Kit (Advanced Analytical, #DNF-474) and measured using a Qubit dsDNA HS Assay Kit (Invitrogen, #Q32851) prior to pooling and sequencing using the Illumina NextSeq 500 platform using a custom primer and the High Output v2 kit (75 cycles) (Illumina, #FC-404-2005). The library loading concentration was 2.4 pM, and the sequencing configuration was as follows: R1 21c / index i7 8c / index i5 8 c / R2 55c.

In parallel, the same cells were seeded in four independent 96well plates and imaged after 14 days of differentiation to quantify their adipogenic potential (see “*In vitro* adipogenic differentiation, chemical treatments and lentiviral infection of hASPCs”).

Analysis of BRB-seq data

Preprocessing

After sequencing and standard Illumina library demultiplexing, the *fastq* files were aligned to the human reference genome GRCh38 using STAR (Version 2.7.3a), excluding multiple mapped reads. Resulting BAM files were sample-demultiplexed using BRB-seqTools v.1.4 and the “gene expression x samples” read, and UMI count matrices were generated using HTSeq v0.12.4.

General methods

Samples with a too low number of reads or UMIs were filtered out. Genes with a count per million greater than 1 in at least 3 samples were retained. Raw counts were then normalized as log counts per million with a pseudo count of 1, using the function *cpm* from *EdgeR*⁸⁸ version 3.30.3. If the samples were from different batches, the raw counts were first normalized using quantile normalization as implemented in *voom* from the package *limma*⁸⁹ version 3.44.3 and then corrected for batch effects using *combat* from *sva* version 3.36.0. PCAs were computed using *prcomp* with the parameters *center* and *scale* set to *TRUE*. Differential expression analyses were performed using *DESeq2*⁹⁰ version 1.28.1 and adding *batch* as a cofactor when necessary.

Scores

Scores were calculated as the sum of the integrated gene expression scaled between 0 and 1 per gene of the mentioned gene lists.

Gene expression heatmaps

Heatmaps display row-normalized expression and were generated using *pheatmap* version 1.0.12. The columns and rows were clustered using the method “ward.2D” of *hclust* of the package *stats*.

Gene set enrichment analysis

Gene set enrichment analysis was performed using the package *clusterprofiler*⁹¹ version 3.16.1.

scRNA-seq of SVF Lin⁻ cells

SVF Lin⁻ cells from different depots and donors were enriched with either FACS or MACS (Table S2) and resuspended in 1% human albumin in DPBS solution prior to be loaded into the Chromium Single Cell Gene Expression Solution (10x Genomics), following the manufacturer’s recommendations targeting a recovery of 4000 to 5000 cells per run. scRNA-seq libraries were obtained following the 10x Genomics recommended protocol, using the reagents included in the Chromium Single Cell 3’ v3 Reagent Kit. Libraries were sequenced on the NextSeq 500 v2 (Illumina) instrument using 150 cycles (18 bp barcode + UMI, and 132-bp transcript 3’ end), obtaining $\sim 5 \times 10^8$ raw reads.

Analysis of scRNA-seq data

Analysis of the datasets individually

Raw fastqs were processed using the default Cell Ranger pipeline (v 2.1.0, 10X Genomics, Pleasanton, CA). The same transcriptome version was used to align all the datasets (GRCh38.92). All the data were then loaded on R (R version 3.6.1). Cells were filtered for the number of Unique Molecular Identifiers (UMIs) and genes using `isOutlier` from the package `scater`, which determines which values in a numeric vector are outliers based on the median absolute deviation (MAD) (nmads set between 3 and 4), and filters for too high a percentage of UMIs mapping to mitochondrial RNA (~10%) or ribosomal RNA (~20%) or too low a percentage of UMIs mapping to protein-coding genes (~80%).

The datasets were first analyzed one by one using the Seurat pipeline.⁹² After cell filtering, only genes expressed in at least 3 cells were kept. The data were scaled for the number of UMIs and features using the function `ScaleData` and the remaining default parameters. The first 50 principal components of the PCA were computed using `RunPCA`, and then evaluated for significance using the `JackStraw` function of Seurat. Only the first PCs successively having a p-value < 0.05 among the top 50 PCs were selected for downstream analysis. Clustering was performed using `FindNeighbors`. The robustness of the clustering was assessed using `clustree` displaying the relationship between the clusters with increasing resolution. Differential expression analysis was computed using the `FindAllMarkers` function of Seurat for the selected clustering. Only genes detected as differentially expressed ($\log_2FC > \log_2(1.2)$, $p_{adj} < 0.05$) for both the Likelihood-ratio test (test.use = "bimod") and Wilcoxon Rank Sum test (test.use = "wilcox") were selected.

Each sample was processed and sequenced individually, with the exception of the samples PR - D30 and PR - D61. The isolated cells of these two samples and donors were mixed. The cells were identified as belonging to each donor post-processing based on two criteria: the results of the clustering of the dataset, which clearly separated the cells from the two individuals, and the expression of *XIST* as the two donors were of the opposite sex. Cells ambiguously assigned to a donor (i.e. having a positive expression of *XIST* while clustering with the cells of the donor patient or the opposite) were filtered out.

Comparison of top markers of individual datasets

For each pair of subpopulations and dataset, the percentage of shared markers between their top 100 differentially expressed genes with the highest FC were calculated and displayed on [Figures S2A–S2C](#).

Scmap

The `Scmap` package²² was used to project the cells of a dataset X onto the identified subpopulations of a dataset Y. Each pair of dataset X, Y and its inverse Y, X were computed. More precisely, the datasets were normalized using the "Single-cell Analysis Toolkit for Gene Expression Data in R" (`scater` package). The data were log normalized using the `logNormCounts` functions using the size factor estimated with `computeSumFactors`. The 1000 most informative features of each dataset were selected using the `selectFeatures` function of `scmap`, which is based on a modified version of the *M3Drop* method. The centroids of each cluster for each dataset were calculated with the function `indexCluster`, and finally, the datasets were projected onto one another using the function `scmapCluster`.

Data integration

The datasets from each individual patient and depot, at the exception of GB-D07 (due to a very low number of captured ASCs), were integrated following the standard workflow of Seurat pipeline. The datasets were normalized in log scale with a scale factor of 10000. The top 2000 highly variable genes were selected using the `FindVariableFeatures` function with the parameter `selection.methods` set to "vst". The anchors were identified using `FindIntegrationAnchors`. The top 2000 variable features identified by `SelectIntegrationFeatures` and the first 60 principal components of the PCA were used as input to perform canonical correlation analysis. The integrated data computed by `IntegrateData` were then used for dimensionality reduction and clustering based on the first 60 principal components of the PCA. Clustering was computed for different clustering resolutions. The final clustering result was based on the clustering results at different resolutions depending on the robustness of the clusters and the specificity of their differentially expressed markers. Top differentially expressed genes were identified using the `FindConservedMarkers` function of Seurat after setting the default assay to RNA, the adjusted p-values were combined using Tippet's method as implemented by the function `minimump` from `metap` R package (meta.method = `metap::minimump`).⁹³ Only groups of cells with at least 10 cells were tested (min.cells.group = 10). Specifically, for the *IGFBP2+* cell cluster, as we found only a few cells per batch and we focused on that cell type in part of the manuscript, DEGs were further computed using `EdgeR` and correcting for batch. More precisely, genes not expressed in at least 2% of the cells were filtered out using the function `filterByExpr`. After converting the count matrix into a `DGEList` using `DGEList`, the data were normalized with `calcNormFactors`. The design matrix was defined following the formula $\sim 0 + \text{clust} + \text{batch}$, where `clust` corresponds to the cluster of every cell and batch to its dataset (as individually shown on [Figure 2A](#)). The dispersion was estimated using `estimateDisp`. The quasi-likelihood negative binomial generalized log-linear model was fitted using `glmQLFit`, followed by the quasi-likelihood *F*-test `glmQLFtest` contrasting the *IGFBP2+* cluster versus the other clusters (pondered by the number of clusters).

Identification of depot-specific markers for ASCs and PreAs

DEG analysis was performed on the integrated data, by selecting the cells of the population of interest (ASCs or PreAs) and contrasting between all possible pairs of depots using the function `FindMarkers` of Seurat. This is possible as we have 3 replicates for SC, OM, PR, and 2 for MC, however, for the latter, those were coming from two biological samples from the same donor. A set of markers was considered depot-specific when significantly differentially expressed in a depot versus any other depot. A gene was defined as differentially expressed when its average log Fold Change (defined as the average of the log Fold Change in each replicate) was positive and an adjusted *p*-value smaller than 0.05.

Comparison with murine ASPCs

Murine data integration. The integration of five datasets of adult mouse SC and OM ATs^{4,7,11,94} was performed as described in Ferrero et al.⁹ The clustering originally published in Ferrero et al.,⁹ focusing on ASPCs, merged the cells close to endothelial cells into one main cluster. The clustering was here revised to include vascular smooth muscle progenitor cells. For consistency with the human data, the top markers of the subpopulation were computed as defined above. The top markers were ordered by the average of the log₂ Fold Change of each dataset.

Score. Scores of the mouse ASPC subpopulations, mesothelial cells, and vascular smooth muscle progenitor cells were based on their human orthologs and calculated as the sum of the gene expression scaled between 0 and 1 per gene of the top markers (average log₂ Fold Change across batches > 0 and adjusted p-value < 0.05) of each murine ASPC subpopulation (ASCs, PreAs, Aregs, *lfit+*, and *Cilp+* ASCs), mesothelial cells and vascular smooth muscle progenitor cells. The scores were then scaled by the number of genes on each list.

Comparison with the dataset from Emont et al.

The whole human single-nucleus/cell dataset (here reported as “scRNA-seq”) provided by Emont et al.⁵ was downloaded on the single cell portal (study no. SCP1376, All cells). The dataset was then subsetted for the cells defined as ASPC or mesothelium by the authors (as defined in the metadata “cell_type2”), and the PCA was recomputed as well as clustering, tSNE and UMAP with the first 50 PCs as input. First, an *IGFBP2* expression score was computed using the AddModuleScore function. The dataset containing only ASPCs, and mesothelial cells was then split by samples, and the symbol gene IDs were converted to Ensembl ID using the GRCh38 release 92 from the Ensembl gene annotation as reference. The few genes with no corresponding Ensembl IDs were filtered out, and, in the rare case of two corresponding Ensembl IDs, only one was kept. Each sample was log normalized with the default normalization of the *Seurat* package and then scaled for the features selected using SelectIntegrationFeatures with each of the samples of Emont et al.⁵ and our generated single-cell SC and OM datasets as input. The first 50 PCs were computed based on the scaled data. Clustering was performed following the default Seurat clustering pipeline for resolutions spanning from 0.1 to 3. Each sample of the Emont et al.⁵ dataset was then projected on our integration (see [analysis of scRNA-seq data](#), [data integration](#)), using the FindTransferAnchors and TransferData functions of the *Seurat* package with the default parameters.

Trajectory analysis

Trajectory analysis was performed on the integrated normalized data subsetting for omental samples. Potential doublets were excluded from the analysis using DoubletFinder⁹⁵ on each omental scRNA-seq dataset individually. Cells labeled as ASCs, PreAs, *IGFBP2+* cells, Mesothelial cells, and VSMPs were selected. The first 50 PCs were computed using the *pca* function of *scanpy*⁹⁶ and the neighborhood graph was computed with the default parameters (pp.neighbors). The connectivity between our defined cell classifications was computed using the paga function,³⁵ and low-connectivity edges were thresholded at 0.03. We computed the ForceAtlas2 (FA2) graph⁹⁷ using PAGA-initialization (draw_graph). The *Dynverse* package⁹⁸ was used to compute the most variable genes along the branch connecting PreAs and Mesothelial cells through *IGFBP2+* cells (calculate_branch_feature_importance).

FACS sorting of human SVF subpopulations

SVF cells were resuspended in 1% human albumin solution (CSL Behring # B05AA01) in PBS to the concentration of 10⁵ cells/μl, and the staining antibody panels (Table S4) were added in titration-determined quantities. At first, all SC, OM, and PR cells were stained with the OM-specific panel, including mesothelial markers, but since SC and PR SVF cells were consistently negative for the TM4SF1 and MSLN markers over three consecutive experiments, SC and PR cells were only stained with the SC and PR panels, respectively (Table S4). The cells were incubated with the cocktail of antibodies on ice for 30 min protected from light, after which they were washed with 1% human albumin in PBS and stained with propidium iodide (Molecular Probes #P3566) for assessing viability, and subjected to FACS using a Becton Dickinson FACSAria II sorter or a MoFlo Astrios EQ, Cell Sorter - Beckman Coulter. Compensation measurements were performed for single stains using compensation beads (eBiosciences #01-2222-42).

The following gating strategy was applied while sorting non-hematopoietic and non-endothelial cells: first, the cells were selected based on their size and granularity or complexity (side and forward scatter), and then any event that could represent more than one cell was eliminated. Next, the live cells were selected based on propidium iodide negativity, and from those, the Lin⁻ (CD45⁻/CD31⁻) population was selected. For the SC samples, from the Lin⁻ fraction of cells, Lin⁻/CD26⁺, Lin⁻/VAP1^{Low/High}, Lin⁻/DN, and Lin⁻/HHIP⁺ cells were defined against unstained controls and FMO controls. For the PR samples, from the Lin⁻ fraction of cells, Lin⁻/CD26⁺, Lin⁻/VAP1⁺, and Lin⁻/DN cells were defined against unstained controls and FMO controls. For the OM samples, OM-specific subpopulations were first isolated from the Lin⁻ gate as Lin⁻/TM4SF1⁺/MSLN^{Low} and Lin⁻/TM4SF1⁺/MSLN^{High} populations. From the remaining Lin⁻/TM4SF1⁻ gate, we then isolated Lin⁻/TM4SF1⁻/CD26⁺, Lin⁻/TM4SF1⁻/VAP1⁺, and Lin⁻/TM4SF1⁻/DN cells. Acquired FCS files were analyzed using FlowJo software to infer population abundances that were plotted using GraphPad Prism.

In vitro adipogenic differentiation, chemical treatments and lentiviral infection of hASPCs

Cells were seeded for adipogenic differentiation at high density (65k cells/cm²) in 3-5 replicate wells of a 96-well black plate (Corning #353219). After 48h or when cells were confluent for at least 24h, cells were treated with induction cocktail (high glucose DMEM (#61965), 10% FBS, 50 μg/ml Primocin, 0.5 mM IBMX (Sigma #15879), 1 μM dexamethasone (Sigma #D2915), 1.7 μM insulin (Sigma #19278), 0.2 mM indomethacin (Sigma #17378) for 7 days, followed by a maintenance cocktail (high glucose DMEM, 10% FBS, 50 μg/ml Primocin, 1.7 μM insulin) for another 7 days. No medium refreshment was performed between these two timepoints. For the chemical treatments, the above-mentioned differentiation and maintenance cocktails were supplemented with the recombinant

IGFBP2 protein at 2nM (R&D, #674-B2-025), recombinant IGF-I protein at 10nM (Sigma, #I3769), recombinant IGF-II protein at 10nM (R&D, #292-G2-050), Blocking anti-human IGFBP2 antibody (scavenging) 1 μ g/ml (R&D, #AF674) and Echistatin 100 nM (R&D, #3202). Chemicals were added to both induction and maintenance cocktails except for Echistatin which was added to the induction cocktail only and withdrawn 48h after induction since inhibiting the integrin receptor resulted in cell detachment when Echistatin was kept in culture for longer periods than 48h. In the Echistatin mixed with IGFBP2 condition, only IGFBP2 was kept after 48h. IGFBP2, IGF-I, and IGF-II were first titrated at the concentrations shown in [Figures S7E and S7F](#).

For lentiviral transduction of hASPCs, our protocol was based on recently published optimization efforts.⁹⁹ In brief the SVF from SC AT was collected and cells were seeded. On their first passage, cells were seeded in 6-well plates at a density of 0.2 million cells/well. The following day, the medium was exchanged with 1 mL of fresh growth medium for viral transduction. Lentiviruses were then added to the media at MOI 3, together with 1 mg/ml Lentiboost (SIRION Biotech) and 100 mg/ml of protamine sulfate (Sigma-Aldrich). After 24 hours, fresh media was added. For validation and IGFBP2 secretion studies, 1 ml of fresh growth media was added and, 24 hours later, the media was collected and protein was extracted from cells in order to correct the secretion assay and to evaluate the expression of the IGFBP2 protein in the different groups. As control for secretion assays, a protein transport inhibitor cocktail (eBioscience, #00-4980-93) was used. For differentiation assays, cells were left in growth media until confluence and then differentiation was triggered as described above. Lentiviruses encoding for mGFP (#PS100071V), Myc-DDK (#PS100064V) and Myc-DDK-tagged IGFBP2 (#RC202573L1V) were acquired from Origene Technologies.

Cell proliferation assay

Sorted cells were split into four and seeded in 4 different wells of a 12-well plate and allowed to attach and start to proliferate for 7 to 10 days. One well of each cell population was trypsinized after this period. Cells were resuspended in 1 ml of medium, counted twice using a hemocytometer, and the mean count was used as the baseline number of cells from which cell increase was calculated. The same counting was performed on the remaining wells every two days. The expansion medium was refreshed every two days.

Mixing and transwell experiments

For the mixing experiments, unexpanded Lin⁻ SVF cells were isolated with MACS using Miltenyi LD columns (Miltenyi, #130-042-901) on manual mono-MACS separators after staining with magnetic anti-human CD45 and CD31 microbeads (Miltenyi, #130-045-801 and #130-091-935) according to the manufacturer's protocol. MACS-isolated Lin⁻ cells from SC, OM, and PR samples were counted in duplicates and mixed at high density (65k cells/cm²) in 11 ratios from 0 to 100%. After 24h, the cells were induced to differentiate following the adipogenic differentiation protocol. For the transwell experiments, we used 96-well plate format transwell inserts with 0.4 μ m (Corning #CLS3391) pores to allow protein and small molecule diffusion through the membrane, but not cell migration. 96well transwell-receiving plates (Corning #3382) were first coated with type I collagen (Corning #354249) 1:500 in DPBS before use to facilitate cell adhesion. Sorted donor OM subpopulations and expanded receiver SC and PR SVF-adherent cells were plated and expanded separately onto the top transwell insert and the bottom receiving plate, respectively. When confluent, the transwell insert was put in contact with the receiver plate, and all cells were induced to differentiate following the listed differentiation protocol.

Enzyme-linked immunosorbent assay (ELISA)

For the supernatant measure, cells were expanded for two passages and seeded into a 6well plate. Once confluent, the expansion medium was aspirated, and wells were washed twice with PBS to ensure residual serum, dead cell and protein removal. 2ml of OPTI-Pro serum-free medium (Thermo, #12309050) was added to each well and incubated with the cells at 37°C for 48h. After incubation, SFM medium was harvested, spun for 10 min at 4°C max speed to clear potential cell debris. Cleared supernatant was aliquoted and stored at -80°C until further usage. For the whole AT IGFBP2 secretion assays, three times 200-400 mg of OM AT were put in 500 μ l of DPBS (Gibco #14190169) and incubated at 37°C for 24, 48 and 72 hours. After incubation, DPBS was harvested, spun for 10 min at 4°C max speed to clear potential cell debris and stored at -80°C until further usage. The Anti-human IGFBP2 ELISA kit (Sigma, #RAB0233-1KT) was used to quantify IGFBP2 protein in the supernatants according to the manufacturer's recommendations. Before loading samples on the ELISA membranes, the total protein concentration was quantified using the Qubit™ Protein Broad Range assay kit (Thermo, #A50669) and 300 ng of total protein was added per reaction. Incubation of samples with primary antibodies was performed O/N at 4°C. At the end of the assay, absorbance was read at 450 nm using a SPARK® Microplate reader.

Immunohistochemistry

Human AT biopsies were washed twice in PBS to remove excess blood and divided in 50 to 100 mg for fixation in 4% PFA (paraformaldehyde, electron microscopy grade (VWR #100504-858)) for 2 hours at 4°C with gentle shaking. Next, the tissue was washed with PBS and incubated with 30% sucrose O/N at 4°C with gentle shaking. Cryoblocks were prepared using Cryomatrix (Thermo Fisher Scientific #6769006), and 25- μ m sections were generated using a Leica CM3050S cryostat at -30°C. The tissue was air-dried for 30 minutes at -20°C in the cryostat itself, then 1h at RT. Slides were additionally fixed 10 min in 4% PFA at RT, washed two times 5 minutes with PBS, permeabilized at RT with 0.25% TritonX100 (Sigma #T9284) for 10 minutes, washed twice with PBS again and antigen blocking was performed at RT for 30 minutes with 1% BSA in PBS. Primary antibodies (anti-TM4SF1, anti-MSLN, anti-PLIN1) in 1% BSA were applied O/N at 4°C with gentle shaking following the titrations indicated in [Table S5](#). The following day, after two PBS washes, and quick 1% BSA dip, the secondary antibody (anti-rabbit AF-647) in 1% BSA was applied for 40 minutes at RT following the titrations in [Table S5](#). Nuclei were stained with 1 μ g/ml DAPI (Sigma #D9564) for 10 minutes and washed twice in PBS prior to

mounting with Fluoromount G (Southern Biotech #0100-01). The slides were then imaged with a Leica SP8 Inverted confocal microscope (objectives: HC PL Fluotar 10x/0.30 air, HC PL APO 20x/0.75 air, HC PL APO 40x/1.25 glyc, HC PL APO 63x/1.40 oil). The results presented in [Figures 5K and 5L](#) were replicated in at least three independent experiments. We note that we also verified that the signal we detected is not the result of autofluorescence of the AT or from unspecific binding of secondary antibodies ([Figure S5D](#))

RNAscope

RNAscope Multiplex Fluorescent V2 assay (Bio-technie, Cat. No. 323110) was performed according to manufacturer's protocol on 4 μ m paraffin sections. They were hybridized with either Hs 3plex positive control (Bio-technie, Cat. No. 320861), the 3Plex negative control (Bio-technie, Cat. No. 3200871) or a combination of the following probes Hs IGFBP2-C1 (Bio-technie, Cat. 313061), Hs MSLN-C2 (Bio-technie, Cat. 413101-C2), Hs DPP4-C3 (Bio-technie, Cat. 477541-C3) at 40°C for 2 hours. The channels were revealed with TSA Opal570 (Akoya Biosciences, Cat. No. FP1488001KT) for C1, TSA Opal520 (Akoya Biosciences, Cat. No. FP1487001KT) for C2 and TSA Opal650 (Akoya Biosciences, Cat. No. FP1496001KT) for C3. Tissues were counterstained with DAPI and mounted with Prolong Gold Antifade Mountant (Thermo Fisher, P36930). Experiments were repeated 3 times.

Protein analyses

To obtain protein extracts, cells were washed with ice-cold PBS and collected in RIPA buffer (Sigma-Aldrich, #20-188) containing protease and phosphatase inhibitors (Roche, #11873580001 and #04906837001, respectively) and transferred into an eppendorf in ice. Then, the whole volume was passed through a 25G syringe 5 times and left on ice for 10 minutes. Finally, cells were centrifuged at 12000g in a refrigerated centrifuge (4°C) for 10 minutes. The pellet was discarded and the supernatant was then used for western blot applications. For signaling studies, the recombinant IGFBP2 (2 nM) and insulin (10 nM) treatments lasted for 2 hours prior to protein extraction. In the corresponding groups, echistatin (100 nM) was added 30 minutes before the start of the IGFBP2 or insulin treatments. Western blots were performed as described previously,¹⁰⁰ and the antibodies used are listed in the [key resources table](#).

Imaging and quantification of *in vitro* adipogenesis

On the 14th day of differentiation, cells were either fixed with 4% PFA (EMS, #15710) and stained at a later timepoint or live-stained with fluorescence dyes: Bodipy 10 μ g/ml (boron-dipyrromethene, Invitrogen #D3922) for lipids and Hoechst 1 μ g/ml (Sigma, #B2883) for nuclei. Cells were incubated with the dyes in PBS, for 30 min in the dark, washed twice with PBS, and imaged. If the imaging was performed on live cells, we used FluoroBrite DMEM (Gibco # A1896701) supplemented with 10% FBS as acquisition medium. Given substantial variation in the extent of lipid accumulation by the tested cell fractions (within the same well but also across technical replicates), the imaging was optimized to cover the largest surface possible of the 96 well. Moreover, a z-stack acquisition in a spinning-disc mode and Z-projection were performed in order to capture the extent of *in vitro* adipogenesis with the highest possible accuracy. Specifically, the automated platform Operetta (Perkin Elmer) was used for imaging. First, 3–6 z-stacks were acquired for every field of view in a confocal mode of the microscope in order to produce high-quality images for downstream z-projection and accurate thresholding. Next, 25 images per well were acquired using a Plan Neofluar 10x Air, NA 0.35 objective for the transwell-receiving plates or 20x air objective NA 0.8 for normal 96w plates (Falcon, #353219), with no overlap for further tiling and with the aim of covering the majority of the well for an accurate representation of lipid accumulation (see Methods in Saalbach and Anderegg¹⁶). The lasers were set in time exposure and power to assure that in both the Hoechst and the Bodipy channels, the pixel intensity was between 500 and 4000, and in all cases at least two times higher than the surrounding background. The images, supported by Harmony software, were exported as TIFF files. They were subsequently tiled, and Z-projected with the maximum intensity method. To accurately estimate and represent differences in adipocyte differentiation, a quantification algorithm for image treatment was developed in collaboration with the EPFL BIOP imaging facility. In brief, image analysis was performed in ImageJ/Fiji, LDs (yellow) and nuclei (blue) images were filtered using a Gaussian blur (sigma equal to 2 and 3, respectively) before automatic thresholding. The automatic thresholding algorithm selections were chosen based on visual inspection of output images. The area corresponding to the thresholded lipid signal was then divided by the area corresponding to the thresholded nuclei area and used to calculate the Adiposcore (totalLipidArea/totalNucleiArea). In the figures, representative blown-up cropped images of each sample are shown. To reduce technical variation across the biological replicates (different donors), adiposcores were normalized to the average adiposcore of the indicated control when we compared conditions within highly differentiating lines like SC and PR. Adiposcores were compared without normalization when we wanted to directly compare adiposcores across depots ([Figures 1C and S1B](#)) or among poorly-differentiating samples like OM when the absolute values of adiposcores were < 0.01 ([Figures 4F, 5E, 7J, and 7N–7P](#)).

siRNA-mediated knockdown

To achieve knockdown of IGFBP2, direct transfection was performed on OM SVF Lin⁻/TM4SF1⁺/MSLN⁻ cells using the IGFBP2 IDT, TriFECTA DsiRNAs kit using 3 pooled siRNAs: hs.Ri.IGFBP2.13.1, hs.Ri.IGFBP2.13.2, hs.Ri.IGFBP2.13.3. In brief, after sorting, cells were expanded for one or two rounds, then harvested and plated at mid-low density (45k cells/cm²) and allowed to adhere. The following day, transfection mix was prepared as Opti-MEM medium (Invitrogen #31985062), 1.5% Lipofectamine RNAiMAX (Invitrogen #13778150) and 20 nM of the pooled siRNAs. In the transfection mix, lipofectamine-siRNA transfection particles were allowed to form for 15 min at RT with gentle shaking. After incubation, the transfection mix was diluted 10 times (to a final concentration of siRNA of 2 nM) in MEMalpha GlutaMax medium (Gibco #32561037) supplemented with 2.5% human platelet lysate (Sigma #SCM152), w/o

antibiotics and exchanged to the plated cell medium. After 48h, medium was changed to differentiation medium (for the transwell assay), with serum free medium (for ELISA validation) or directly taken in TRIzol (for qPCR validation).

RNA isolation and qPCR

Expanded OM and SC SVF-adherent, OM SVF Lin⁻/TM4SF1⁻/MSLN⁻, OM SVF Lin⁻/TM4SF1⁺/MSLN⁻ cells as well as cells subjected to siRNA-mediated knockdowns 48h post-transfection were collected into TRIzol (Sigma, #T3934). The direct-zol RNA kit (Zymo Research #R2062) was used to extract RNA, followed by reverse transcription using the SuperScript II VILO cDNA Synthesis Kit (Invitrogen # 11754050). Expression levels of mRNA were assessed by real-time PCR using the PowerUp SYBR Green Master Mix (Thermo Fisher Scientific #A25743). mRNA expression was normalized to the Hprt1 gene. Primer sequences used: *IGFBP2* – Fw CGAGGGCACTTGTGAGAAGCG, Rv TGTTTCATGGTGCTGCCACGTG; *HPRT* – Fw CAGCCCTGGCGTCGTGATTA, Rv GTGATG GCCTCCCATCTCCTT.

QUANTIFICATION AND STATISTICAL ANALYSIS

The experiments were not randomized, and the investigators were not blinded in experiments. The paired Student's *t*-test was used to determine statistical differences between two groups, with the null hypothesis being that the two groups are equal. Multiple comparisons were corrected using false discovery rate (FDR) correction. When specified, one-way ANOVA or RELM test followed by Tukey honest significant difference (HSD) post hoc correction was applied, the null hypothesis being defined so that the difference of means was zero. (Adjusted) **p*-value < 0.05, ***p*-value < 0.01, ****p*-value < 0.001 were considered statistically significant. All boxplots display the mean as a dark band, the box shows the 25th and 75th percentiles, while the whiskers indicate the minimum and maximum data points in the considered dataset excluding outliers. All bar plots display the mean value and the standard deviation from the mean as error bar.